Fluid Fluxing and Accumulation Drive Decadal and Short-Lived Explosive Basaltic Andesite Eruptions Preceded by Limited Volcanic Unrest

S Utami, F Costa, Ph Lesage, Patrick Allard, H Humaida

JOURNAL OF PETROLOGY

Journal of Petrology, 2021, Vol. 62, No. 11, 1–29
https://doi.org/10.1093/petrology/egab086
Advance Access Publication Date: 08 October 2021
Original Manuscript

OXFORD

Fluid Fluxing and Accumulation Drive Decadal and Short-Lived Explosive Basaltic Andesite Eruptions Preceded by Limited Volcanic Unrest

S. B. Utami[1,*], F. Costa[1,2], Ph. Lesage[3], P. Allard[4], and H. Humaida[5]

[1]Asian School of the Environment, Nanyang Technological University 50 Nanyang Avenue, N2-01B-27 Singapore, 639798; [2]Earth Observatory of Singapore, Nanyang Technological University 50 Nanyang Avenue, N2-01A-15 Singapore, 639798; [3]ISTerre, Université Savoie Mont Blanc-Université Grenoble Alpes-Université, Gustave Eiffel, CNRS, IRD, 38000, Grenoble, France; [4]Institut de Physique du Globe de Paris, Université de Paris, CNRS UMR71541, Rue Jussieu, 75005, Paris, France; and [5]Jl. Cendana No.15, Semaki, Kec. Umbulharjo, Kota Yogyakarta, Daerah Istimewa Yogyakarta 55166, Indonesia

*Corresponding author: E-mail: sri.budhi.utami@gmail.com

Received 26 February 2021; Revised 19 August 2021; Accepted 6 October 2021

Abstract

Some volcanoes are known for repeatedly producing explosive but short-lived eruptions (< half a day) every decade or so. These eruptions are often preceded by limited unrest signals and short run-up times to eruption (a few hours to months), and thus they are difficult to anticipate. Some well-documented examples are the 1990 and 2014 eruptions of Kelud volcano in Indonesia, or the 2015 Calbuco eruption in Chile. Here we interrogate the rock record and obtain insights into the processes and pre-eruptive conditions that led to the 1990 Kelud eruption, which we integrate with monitoring data (seismicity, lake temperature and hydro-acoustics, sulfur emissions) towards a conceptual model for this type of events. Mineral-melt geothermobarometers indicate that the basaltic andesite magma carried a crystal cargo from as deep as 15–19 km, and reached volatile saturation at 4–9 km with 2–4 wt.% water in the melt. The textures and compositional zoning of orthopyroxene and plagioclase do not support intrusion of more primitive magma as the driver for the eruption, and we instead propose that pre-eruptive fluid accumulation and high-temperature fluid fluxing from depth (likely dominated by CO_2) played a major role in priming the eruption to occur. Such pre-eruptive gas accumulation is also supported by mass balance calculation of the emitted excess SO_2 gas. Mg-Fe diffusion profiles in reversely zoned pyroxenes constrain timescales of weeks to months before eruption for fluid addition to the reservoir, and such events may be recorded in the monitoring signals, especially in the change of hydroacoustics and water lake temperature, and probably in the seismic swarms. We propose that fluid exsolution and accumulation in the shallow reservoir plays a crucial role in modulating and triggering short-lived explosive eruptions with brief unrest at Kelud and probably other volcanoes worldwide.

Key words: volcano monitoring; magma storage conditions; diffusion timescales; Kelud; Kelut

INTRODUCTION

Explosive eruptions can generate lethal hazards, and thus special attention is needed to monitor and properly interpret the signs of unrest in anticipation of the eruption (Jolly and de la Cruz, 2015). Yet for many eruptions, dedicated volcano monitoring efforts are not enough to anticipate their explosivity, when the eruption will occur, and how it will progress with time. This is partly because the relationship between the magmatic processes controlling the eruptions and associated unrest patterns are poorly understood. Explosive eruptions can often be preceded by a wide range of unrest patterns, from abrupt to gradual to progressive changes in precursory signals over times les varying from a few days to years before eruption, for example in Merapi 2006 vs. 2010 (Indonesia) (Ratdomopurbo *et al.*, 2013; Surono *et al.*, 2012). Some explosive eruptions are preceded by exceptionally short run-up times (a few hours to a few weeks), which makes it extremely challenging for civil protection authorities

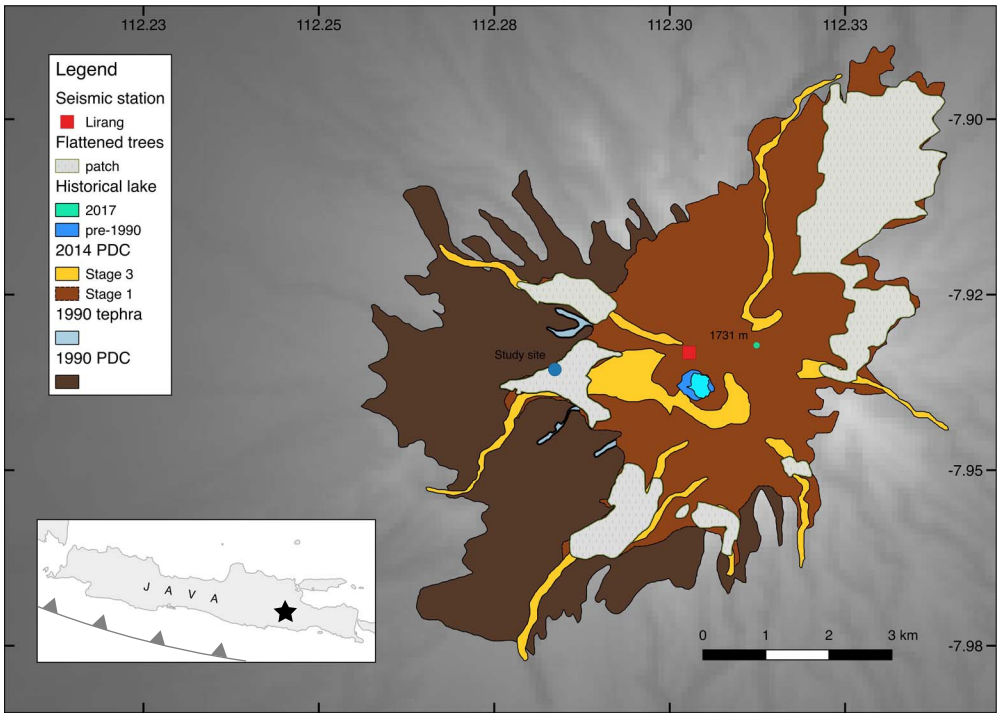

Fig. 1. Map of 1990–2014 volcanic deposits at Kelud volcano showing the distribution of the 1990 deposits from tephra fall and pyroclastic density currents (PDC) as documented by Bourdier *et al.* (1997). These are overlain by pyroclastic density flows from the 2014 eruption (defined as Stage 1 and 3). Regions of flattened trees were digitized from Maeno *et al.* (2017). The Lirang seismic station was the single station with interpretable seismic data in 1990 (Lesage & Surono, 1995). Inset map shows the location of Kelud in the island of Java, Indonesia.

to advise communities, given the limited time to activate mitigation plans.

Kelud volcano, located in East Java (Indonesia) is part of the Sunda arc volcanoes, and a good example of a volcanic system that has produced two explosive eruptions that were preceded by short unrest in 1990 and 2014. For example, before the event in 2014, volcano-tectonic earthquakes abruptly spiked starting from 3 February, dissipating until 10 February, before a final spike in seismicity occurred a couple of hours before the eruption at 22:50 on 13 February (e.g. Cassidy *et al.*, 2019; Hidayati *et al.*, 2018; Maeno *et al.*, 2016). Such a pattern is observed at other subduction zone volcanoes in the world (Passarelli and Brodsky, 2012, and references therein). Calbuco volcano in Chile, which erupted explosively in 2015, had very short run up times of seismicity a few hours before its first explosive phase that produced a volcanic cloud column >20 km tall (Arzilli *et al.*, 2019; Morgado *et al.*, 2019a, 2019b; Pardini *et al.*, 2018).

The link between magmatic processes, unrest signals and the explosive dynamics of these eruptions can be elucidated by combining various types of information: the whole-rock, mineral compositions, and textures combined with timescale indicators (e.g. Albert *et al.*, 2016; Kahl *et al.*, 2013; Rasmussen *et al.*, 2018); thermobarometric constraints and geophysical models (Chiarabba *et al.*, 2004; Patanè *et al.*, 2003; Widiyantoro *et al.*, 2018); petrological estimates of magma degassing compared to satellite measurements of volatile emissions (Caricchi *et al.*, 2014; Jay *et al.*, 2014); petrological indicators of magma volume, timescales and processes compared to unrest signals from monitoring records (Cheng and Costa, 2019; Kahl *et al.*, 2011). Such integrative approaches have been applied to investigate the processes and mechanisms that lead to different eruptions at a variety of volcanoes (e.g. Costa *et al.*, 2020), including Mt Etna (Kahl *et al.*, 2013), Eyjafjallajökull (Pankhurst *et al.*, 2018), Mt. St. Helens (Saunders *et al.*, 2012), Ruapehu (Kilgour *et al.*, 2014), Shishaldin (Rasmussen *et al.*, 2018), Piton de la Fournaise (Albert *et al.*, 2019), or Kilauea. For many of these examples renewed mafic magma injection is proposed to be the main driving mechanism for the eruption.

Here we provide new constraints on the pre-eruptive conditions and the driving mechanism of the 1990 explosive eruption of Kelud, based on detailed investigations of its eruption deposits, minerals, and glass. We also obtain timescales for the magmatic processes which we combine with the instrumentally recorded unrest signals to propose a conceptual model for the eruption. We show that fluid accumulation in the upper parts of the reservoir during years of repose and fluxing of deep fluids that are likely CO_2-dominated may play a key role in promoting and driving the recurrent, short-lived explosive eruptions at Kelud. Such fluid accumulation and fluxing may be recognized in the monitoring signals recorded in a lake water present before the eruption. Our findings may thus be of importance towards a better understanding of future eruptions at Kelud and of analogous events other volcanoes worldwide.

GEOLOGICAL SETTING

Kelud volcano and lake

Kelud is a basaltic andesite stratovolcanic complex located in East Java (Indonesia) as part of the Sunda Arc subduction zone volcanoes, and has been classified as semi-plugged as there is no significant degassing during repose periods (Whelley *et al.*, 2015) (Fig. 1). The current edifice consists of two highly excavated craters (Kawah Dargo being the main one) with a westward opening, surrounded by four crypto-domes (Sumbing, Lirang, Gajah Mungkur, and Umbuk) (Wirakusumah, 1991). The location and age of the nearest

crypto-domes indicate a clockwise shift of eruptive centers over time, from the earliest crypto-dome (Gunung Lirang, 238 ky) to the current crater (Global Volcanism Program, 2013; Wirakusumah, 1991). More distal parasitic domes, such as the Gunung Umbuk show evidence for flank volcanic activity at ~39 kya (Wirakusumah, 1991). The valleys around the volcano are highly incised and steeply dipping, showing that the edifice is being actively eroded. Kelud hosts one of the few neutral pH volcanic lakes in the world, whose volume averaged ~2.5 × 10^6 m^3 prior to the 1990 eruption (Bourdier *et al.*, 1997). Bernard and Mazot (2004) identified two hydrothermal systems feeding the pre-1990 crater lake: a deep Li-B-enriched alkali-chloride hydrothermal system, and a shallow Ca-Mg sulfate dominated hydrothermal system. The neutral pH indicates that an impermeable barrier exists somewhere between the magma reservoir and the shallow conduit of Kelud. After the devastating 1919 eruption (5160 casualties), a drainage tunnel system was constructed to drain the lake level and reduce the hazards from lahars during future eruptions. This drainage system was further deepened after the 1966 eruption (Caudron *et al.*, 2012).

Historical eruptions and hazards from Kelud

Kelud has erupted around 34 times since 1000 CE and all events were highly explosive except for two dome extrusions in 1920 and 2007 (Global Volcanism Program, 2013). Most eruptions generated a range of hazards, including lahars, landslides, ash fall, ballistics, and pyroclastic density currents (Global Volcanism Program, 2013). Lahars generated by the mixing of eruptive deposits with lake water have caused most of the fatalities, killing 5160 people in 1919, and up to 10 000 people in 1586 (Global Volcanism Program, 2013). Ashfall has produced widespread damage to the surrounding villages and cities (e.g. Blake *et al.*, 2015; Bourdier *et al.*, 1997; Pardyanto, 1990; Williams *et al.*, 2020), with roof collapse due to ash accumulation killing 32 people in 1990. Ash also forms unconsolidated deposits that become washed down the flanks and the steep-sided valleys by heavy rains, forming cold lahars (Thouret *et al.*, 1998). Pyroclastic density currents usually remain confined to inside the crater or proximal areas (Bourdier *et al.*, 1997; Maeno *et al.*, 2016). The last eruption in 2014 generated a 17-km high volcanic column, promoting ash circulation within the troposphere for several months (Kristiansen *et al.*, 2015; Vernier *et al.*, 2016) and causing extensive damage to infrastructure networks across multiple cities in Java (Blake *et al.*, 2015). Despite its suddenness and widespread impact more than 160 000 people were evacuated in less than two hours, thanks to the high level of preparedness and coordination by the Centre for Volcanology and Geological Hazard Mitigation (CVGHM) (Andreastuti *et al.*, 2016).

The 1990 eruption

This eruption ejected a total volcanic volume of 0.13 km^3 dense rock equivalent (DRE) (Bourdier *et al.*, 1997), and released a total of ~170 kt of SO_2 into the troposphere according to satellite data (Global Volcanism Program, 2013). The unrest period leading up to the February 1990 eruption of Kelud was characterized by changes of the crater lake, hydroacoustics anomalies, and seismic swarms. According to Vandemeulebrouck *et al.* (2000) the unrest might have started in April 1989 with an increase in baseline of low frequency hydroacoustics signals, probably due to the onset of gas rising up and early boiling of the lake water. Four main stages can be recognized in the sequence of events that led to the 1990 eruption of Kelud (Table S1). All reported times refer to local time (GMT + 7):

1. **Main unrest phase (November 1989–January 1990):** this was marked by an increased number of daily earthquakes and the appearance of two seismic swarms in December 1989, and then January 1990. Lesage & Surono (1995) attributed these swarms to fracturing of a brittle plug blocking the volcano conduit. Changes were also observed in the chemistry, pH, and color of the lake (Badrudin, 1994; Kadarsetia *et al.*, 2006). The lake bottom and surface temperature increased from 30–60°C and from 30–48°C, respectively (Pardyanto, 1990). Vandemeulebrouck *et al.* (2000) interpreted the increasing hydroacoustic signals in the high-frequency band as due to increased gas bubbling in a convective column, and signals in the ultrasonic frequency bands as related to pressure variations in the hydrothermal system.
2. **Temporary quiescence (January–9 February 1990):** this lasted about three weeks and both seismic and hydroacoustic signals decreased to their background levels.
3. **Escalation (9–10 February 1990):** renewed unrest suddenly started after midnight on 9 February with >400 low magnitude earthquakes recorded until 9:00 am on 10 February, the day of the eruption (Lesage & Surono, 1995). In response, the Volcanological Survey of Indonesia ordered an evacuation at 10:00 am (Pardyanto, 1990).
4. **The eruption (10 February 1990):** The eruption started at 11:41 am, with seven phreatomagmatic explosions in one hour. From 12:35 pm, it then rapidly developed as a sub-Plinian magmatic phase with a 10-km high column and lasted until 5:00 pm and its collapse generated pyroclastic flows (Global Volcanism Program 1990; Pardyanto 1990; Lesage & Surono 1995). Tephra of lapilli size fell on Margomulyo Volcano Observatory, about 7 km west of the crater, until 5:00 pm, and ash continued to fall during the night. After this major phase, smaller discrete explosive outbursts occurred on the 11 and 12 February that produced incandescent tephra and lightning (Global Volcanism Program, 1990). The main phase of the eruption ended around March 1990 (Global Volcanism Program, 2013), having completely emptied the crater lake and generated syn-eruptive hot lahars.
5. Heavy tropical rainfalls subsequently remobilized the fresh pyroclastic deposits to produce 33 cold lahar episodes until 28 March (Thouret *et al.*, 1998). After the eruption, a new magmatic plug had solidified in the excavated crater and a new lake gradually reformed (Bourdier *et al.*, 1997). According to the Volcano Survey of Indonesia, the eruption ended at the end of March 1990 (Global Volcanism Program, 1990).

METHODOLOGY

Sampling strategy

The studied rock samples were taken from a vertical outcrop in the southwestern part of Kelud's main crater that provides access to deposits from the 1951 to 1990 eruptions (Fig. 2). The studied outcrop was protected by dense vegetation before the 2014 eruption, and afterwards, by trees blown down by that eruption (Maeno *et al.*, 2016).

The 1951 deposit is made of beds of ash and blocks, gently dipping downward away from the main crater, and contains both unaltered white pumices (> 64 mm), oxidized red pumices, and dark ones partially covered by soil and organic matter. Entrained lithic clasts (< 64 mm) and charcoal are minor components. A paleosol

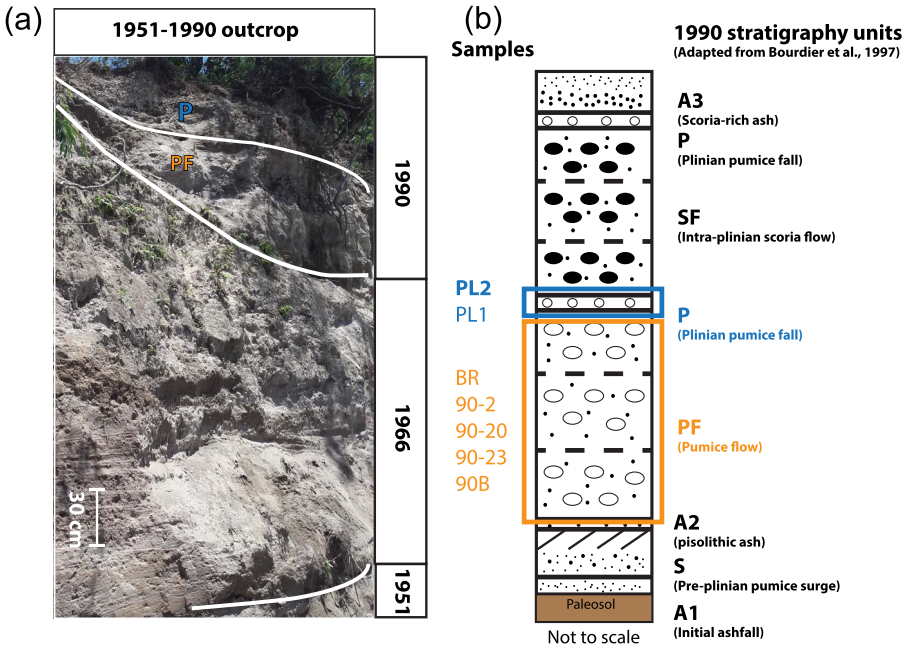

Fig. 2. (a) Photograph of the main 1990 outcrop sampled for this study, overlying the previous deposits from 1966 and 1951 eruption. (b) schematic diagram of the 1990 stratigraphic units showing our sample distribution and names (adapted from Bourdier *et al.*, 1997). All samples except for PL2 derive from the main eruption stage in the pumice flow and fall deposits, while PL2 (in bold) representing the late eruption stage is found embedded in the pumice fall deposit. Only the pumice fall (P) and pumice flow (PF) units are shown in the outcrop photograph.

horizon separates the 1951 eruption deposit from the overlying 1966 eruption deposit. The latter deposit consists of massive to weakly bedded ash and block layers, containing bomb-sized pumice blocks and lithic clasts of comparable sizes. The 1966 pumices are light grey to white porphyritic blocks. Another paleosol horizon separates products from the 1966 and 1990 eruptions. The 1990 deposit gently dips upward away from the crater and consists of a mixture of ash and poorly to moderately-sorted grey to white pumice blocks, together with entrained charcoal and lithics. Pumice clasts range from sub-rounded lapilli to bomb-sized pumices blocks (up to 15 cm), embedded in a mixture of ash and smaller pumice fragments. Lithic ejecta are sub-rounded to sub-angular porphyritic andesites. We interpreted this lens as the *pumice flow layer* previously described by Bourdier *et al.* (1997). This layer is overlain by an upward dipping, clast-dominated bed containing sub-rounded to rounded lapilli- to bomb-sized pumice clasts, as well as lithics. We interpret this upper bed as the *pumice fall layer* described by Bourdier *et al.* (1997) in their composite stratigraphy.

We found two types of pumices within the 1990 deposits: (1) a volumetrically prevalent, light and vesicular pumice in both the pumice flow and fall deposits, and (2) a volumetrically minor, relatively dense but still vesicular pumice in the pumice fall deposit only. Combining our observations with the composite stratigraphy of Bourdier *et al.* (1997), we consider the prevalent pumice component as representative for the main eruption stage, whereas the minor pumice component represents the late eruption stage. Thereafter, we refer to these samples as 'main-stage' and 'late-stage'. We studied six pumice samples from the main-stage and one from the late-stage. Our samples were collected from the outcrop described above during a field campaign in October 2017 and were complemented by samples previously collected by Humaida (2013) that we interpreted to be main-stage pumices. Lithic clasts are fragments of either past lava flows excavated during the eruption or fragments of the plug that blocked the conduit (Lesage & Surono, 1995). The 1990 deposit stratigraphy closely resembles that of the subsequent 2014 eruption, compiled by Maeno *et al.* (2019) and Goode *et al.* (2018). We did not find scoriaceous pumice clasts in the 1990 deposit, but Bourdier *et al.* (1997) found scoria deposits in other outcrops, which were included in their composite stratigraphic column. Scoria was also produced during the 2014 eruption and lapilli-sized clasts were found around the crater floor.

Analytical methodology

Bulk sample characterization

Point counting was conducted on standard polished petrographic thin sections to determine the areal proportions of minerals and groundmass (> 1400 point per thin section), using a Pelcon mechanical point counting stage, and the JMicrovision software on optical images of the thin sections. Whole-rock major and trace element compositions were analyzed using X-Ray Fluorescence (XRF) with fused lithium methaborate/tetraborate discs—and inductively coupled plasma mass spectrometer (ICP-MS) at the Activation Laboratory in Ancaster, Ontario (Canada) following the approach outlined in Norrish and Hutton (1969). There was no alteration on the samples, and thus no additional steps were taken other than cutting the pumices into small 50 × 40 mm billets needed for whole rock analyses. All other preparation steps, including crushing and powdering, was done at Activation Laboratory.

Textures, mineral and glass chemistry

Minerals and textures of interest were characterized and imaged using the JEOL JSM-7800F field emission scanning electron microscope (SEM) at the Asian School of the Environment, Nanyang

Technological University (NTU), Singapore. We used an accelerating voltage of 15 kV, 20 nA current to obtain back-scattered electron (BSE) images of various parts of the sample. Minerals and glasses were analyzed in both spot and traverse modes using a JEOL-JXA 8530F field emission EPMA at the Facility for Analysis Characterization Testing & Simulation (FACTS) at NTU. We determined the major element composition of plagioclase (Plag, $n = 388$), orthopyroxene (Opx, $n = 1628$), clinopyroxene (Cpx, $n = 639$), Fe-Ti oxides (magnetite – Mag, $n = 53$; ilmenite – Ilm, $n = 35$), and amphibole (Amph, $n = 20$). Quartz (Qz) was identified but not analyzed. Point and traverse analyses of Opx and Cpx were made with a focused beam of about 1 mm, accelerating voltage of 15 kV and a current of 20 nA. The relative errors for pyroxene analysis are 0.2–6% for Si, Al, Ca, Mg, Fe, and Mn; and 1–64% for Na, Ti, and K. For plagioclase, Mag, and Ilm analysis we used the same beam size and accelerating voltage, but with a 10 nA beam current. Relative errors for Fe-Ti mineral analysis are 0.2–7% for Fe, Ti, and Mg; 2–24% for Mn, Al and Si; and 8–99% for Cr. For Plag analysis, the relative errors are 0.4–4% for Si, Al, Na, Ca, and Fe, whereas for Mg and K, the relative errors are 1–55%. Amph was analyzed with a beam of 1 to 5 mm, a 15 kV accelerating voltage, and a 10 nA beam current. The relative errors are 0.4–6% for all major element oxide contents in Amph, except for Cr_2O_3, where they are 13–62%. The relative error for halogens in Amph are 32–56% for Cl and 19–58% for F. The EPMA standard reference materials for pyroxene and Amph analyses came from P & H (diopside – Si, Ca, Mg; corundum – Al, albite – Na, rutile - Ti, specularite – Fe, rhodonite – Mn, Chromium oxide – Cr, and orthoclase – K, fluorite – F, halite – Cl). The standard reference materials for Plag, came from P & H (albite – Na, Al, Si; wollastonite – Ca, orthoclase – K and olivine – Mg) and Astimex (olivine – Mg, Fe, plagioclase – Ca). The standard reference materials for Fe-Ti oxides came from Astimex (Almandine – Al, Si; titanium – Ti, diopside – Mg, chromium oxide – Cr; magnetite – Fe, rhodonite – Mn).

Chemical indicators used to characterize the minerals were calculated from standard structural formulae (Deer *et al.*, 1992). Pyroxenes are characterized by Mg-number ($Mg\# = 100 \times Mg / [Mg + Fe^*]$ in mol, where Fe∗ is total iron as Fe^{2+}), and their proportions of wollastonite ($Wo = 100 \times Ca / [Ca + Mg + Fe^*]$ in mol), enstatite ($En = 100 \times Mg / [Ca + Mg + Fe^*]$ in mol), and ferrosilite ($Fs = 100 \times Fe^* / [Ca + Mg + Fe^*]$ in mol). Plag composition is described with the anorthite content ($An = 100 \times Ca / [Ca + Na]$ in mol). For magnetite we computed the ülvospinel component, $X_{usp} = 3 \times Ti / (Ti + Fe^*)$, and for ilmenite, $X_{Ilm} = 2 \times Ti / (Ti + Fe^*)$, following Sauerzapf *et al.* (2008). For amphibole, we used the structural formulae of Leake *et al.* (1997) as included in Ridolfi *et al.* (2010).

Glass inclusions hosted in Cpx and interstitial glass were analyzed using a defocused beam of 10 mm, an accelerating voltage of 6 kV and a current of 5 nA. The following elements were analyzed: Si, Al, Ca, Na, K, Fe*, Mg, Mn, Ti, P, Cl, and S, with Na analyzed first to account for Na migration during analyses. Melt inclusion compositions were corrected for post-entrapment crystallization of the host mineral along the melt inclusion walls (e.g. Bucholz *et al.*, 2013; Esposito *et al.*, 2014; Gaetani & Watson, 2000). A hypothetical groundmass composition of each sample was obtained by subtracting the median major oxide compositions of the phenocrysts (Plag + Opx + Cpx + Mag), weighted to their modal abundances, from the whole-rock composition. For a few samples whose whole rock compositions was not available (samples 90–2 and 90–20), we used the average composition of all 1990 samples reported by Humaida (2013). Such composition was used where appropriated to calculate some intensive variables of the magma.

Geothermobarometry and magma storage conditions

Mineral geothermobarometers

The pre-eruptive conditions of magma storage (temperature, T; pressure, P; oxygen fugacity, fO_2, and melt water content) were inferred using a combined approach of rhyolite-MELTS thermodynamic software (Gualda *et al.*, 2012), nine mineral/melt geothermobarometers, oxybarometers, and a hygrometer, as described below. Reliable application of these geothermobarometers and volatile calculations require assessment of equilibrium. For mineral-mineral pairs, calculations were done using the core–core or rim–rim compositions of touching grains, where available. For mineral-melt pairs from the main-stage pumices, crystal core compositions were paired with the whole-rock compositions, and crystal rim compositions were paired with the measured interstitial glass composition. For late-stage samples, rim and microlite compositions were paired with the calculated groundmass composition rather than the measured interstitial glass, because we found that the latter was too evolved to be in equilibrium with the phenocrysts.

Pyroxene-melt equilibrium was tested using the Mg/Fe* distribution coefficient (*Kd*) defined as:

$$Kd_{crystal-melt} = \frac{X_{Fe}^{crystal} X_{Mg}^{melt}}{X_{Mg}^{crystal} X_{Fe}^{melt}} \quad (1)$$

where X is the mol fraction for the relevant mineral–melt and mineral–mineral pairs using $Kd_{Cpx-melt} = 0.28 \pm 0.08$ and $Kd_{Opx-melt} = 0.29 \pm 0.06$ (Putirka 2008). For Opx- and Cpx-melt geothermometers (equations 28a and 33 in Putirka (2008), respectively), we fixed the Fe^{2+}/Fe_{total} of the melts at the fO_2 reaction buffer constrained by Fe-Ti oxides equilibria as determined in late-stage pumices (Sauerzapf *et al.*, 2008). We also added 3 wt.% water into the melt according to hygrometer results (see below). Varying the water content in the melt by ± 1 wt.% changes the calculated temperature by <15°C for pyroxene-melt geothermometers. The standard errors on temperatures estimated from the Cpx-melt and Opx-melt geothermometers are ± 42°C and ± 48°C (Putirka, 2008), respectively. For all pyroxene-based geothermometers, the pressure was fixed at 100 MPa. A pressure change of ± 100 MPa results in a temperature change of ± 5°C. No adjacent Opx-Cpx crystals appear to be in equilibrium using the *Kd* criterion of Putirka (2008). Instead, we used the QUILF algorithm of Andersen *et al.* (1993) and we only report the temperatures for which the calculated and expected pyroxene compositions are similar within analytical uncertainty and give T errors <25°C.

For the amphibole-melt geothermobarometry, using the Mg-Fe* $Kd_{Amph-melt}$ of Putirka (2016) resulted in a very wide range of possible equilibrium melts. We thus used an additional equilibrium test based on the exchange of Si/Al (mol) ($Kd_{Amph-melt} = 0.96 \pm 0.04$; Li *et al.*, 2021), from which we verified the Amph phenocrysts to be in equilibrium with the whole rock. We also applied the Amph geothermobarometry formulations of Ridolfi & Renzulli (2012) and Ridolfi *et al.* (2010) and we accepted all results that fulfilled the structural formulae of Ridolfi *et al.* (2010).

The fO_2 and temperature for the late-stage pumices were calculated from co-existing Mag-Ilm pairs and the oxybarometer calibrations of Sauerzapf *et al.* (2008), and Ghiorso & Evans (2008). We also used the Plag-melt hygrometer of Waters & Lange (2015)

to determine the pre-eruptive water content of the melt. For this, we considered the compositions of the crystal rims, and of the interstitial glass, together with the temperatures given by the Opx-melt geothermometer for the main-stage pumices, and by Fe-Ti oxides for the late-stage pumices. The calculated water content, temperature, and interstitial glass compositions were then combined with the H_2O-CO_2 saturation model of Ghiorso & Gualda (2015) in the MagmaSat application to estimate volatile saturation pressures. For some computations we considered the maximum CO_2 concentration (336 mg/kg) measured by Cassidy *et al.* (2016) in plagioclase-hosted melt inclusions of the 2014 products. We recognize that this may not be directly applicable to the 1990 eruption, and that is likely a minimal value for the melt, since no corrections was made for the potential CO_2 present in the bubble (e.g. Bucholz *et al.*, 2013; Gaetani *et al.*, 2012; Lloyd *et al.*, 2013).

Pyroxene diffusion modeling and calculations of timescales

The timescales of Fe-Mg re-equilibration in Opx and Cpx were obtained from our measured crystal zoning profiles and the diffusion model approaches described in Costa *et al.* (2008) and Flaherty *et al.* (2018). A total of 38 reversely zoned crystal profiles were used: 22 in the main-stage samples (Opx = 20, Cpx = 2), and 16 in the late-stage samples (Opx = 14, Cpx = 2). We used the zoning in Mg-number of rim-to-core profiles approximately perpendicular to the crystal *c*-axis (along *a* or *b* axis) since this is deemed to be the slowest diffusion direction and the least affected by 2D or 3D diffusion (cf. Krimer & Costa, 2017). For initial profile geometries, we used sharp step functions across two well-defined compositional plateaus that are close to the observed zoning profile shape and thus have less uncertainty (Costa & Morgan, 2010). We performed independent checks of the geometry and position of initial Mg-number distributions by comparing to Al_2O_3, which is a slower diffusing component and thus likely closer the initial profile that would be related to growth. As a boundary condition we assumed a constant composition at the crystal rim. We thus obtained a range of diffusion timescales around a best fit for each profile with the analytical uncertainty and diffusion coefficients determined following Flaherty *et al.* (2018).

For profiles in Opx crystals we used the Fe-Mg diffusion coefficient formulations of Dohmen *et al.* (2017) including the correction for composition, as well as the formulations of Ganguly & Tazzoli (1994) which give 2–3 times shorter diffusion timescales at the range of composition, temperature, and fO_2 values at Kelud. Fe-Mg zoning in Cpx crystals was modeled by using the diffusion coefficient of Müller *et al.* (2013), assuming isotropic diffusion. A mean rim temperature of $T = 979 \pm 48°C$ was used for modeling according to Opx rim-melt temperatures we have obtained (see below), with the fO_2 buffered at NNO +1 (log $fO_2 = -9.60$) according to the formulation of O'Neill & Pownceby (1993). For the late-stage Opx, we used a mean temperature of $T = 972 \pm 48°C$ calculated from the rim and calculated melt pairs, also with fO_2 at the same buffer (log $fO_2 = -9.70$). Data for modeling the Cpx crystals is from one sample (90–23) for which Cpx-melt temperatures average $1023 \pm 42°C$ for the main-stage and $976 \pm 42°C$ for the late-stage, all according to our geothermobarometry results presented in further sections.

Calculation of exsolved fluid using SO_2 mass balance

We computed the mass of fluid exsolved from the melt by using the petrologic method (Devine *et al.*, 1984). The highest sulphur concentration in Cpx-hosted melt inclusions was taken to represent the pre-eruptive S content of the melt and the sulphur concentration of the interstitial glass to represent the degassed melt. The total amount of sulphur (as SO_2) outgassed during the 1990 eruption is given by the sulphur loss per unit mass of magma normalized to the residual melt proportions and multiplied by the DRE volume of the eruption. We compared our petrologic estimate of the outgassed amount of SO_2 with the total SO_2 emissions measured from space (0.17 Mt; TOMS, Global Volcanism Program, 2013) to evaluate the presence of an exsolved fluid phase prior to eruption (e.g. Costa *et al.*, 2003; Costa *et al.*, 2013; Jay *et al.*, 2014).

RESULTS

Petrology, mineralogy, and geochemistry of main- and late-stage pumices

Whole rock and glass chemistry

The whole rock composition of both, the main- and late-stage pumices is basaltic andesite (Table 2 and Fig. 3a), with 54–56 wt.% SiO_2, a total alkali silica ($Na_2O + K_2O$) of ~4 wt.%, and a K_2O content that straddles the boundary between the low- to mid-K series (Fig. 3b). Other major oxides show limited compositional variability (8–9 wt.% CaO, 2–4 wt.% MgO, 18–19 wt.% Al_2O_3, and 9–10 wt.% FeO*) (Table 2, Fig. 3c–f). Interstitial glass and melt inclusions from the main-stage samples are more evolved than the corresponding whole rock, ranging in composition from dacite to rhyolite (Fig. 3a). The late-stage pumices are slightly more evolved than the main-stage ones, and the interstitial glasses contain <1 wt.% of MgO, FeO* and CaO. The calculated groundmass melts obtained by subtracting phenocrysts from the whole rock are also dacitic (Table S3), and are compositionally intermediate between the whole rock and the measured interstitial glass or melt inclusions. Compositional trends in Harker diagrams of other major oxides (CaO, MgO, FeO, and Al_2O_3) versus SiO_2 are broadly linear and with a negative slope (Fig. 3c–f) which can be due to crystal fractionation and/or mixing between the crystals and melts of different origins (see Fig. S1).

Trace element concentrations in the whole rocks show a pattern typical of island arc magmas (Fig. S2). Primitive mantle-normalized trace element patterns reveal a relative enrichment in fluid mobile large ion lithophile elements (Cs, Rb, Ba, Sr), with a pronounced spike in Pb, and depletion in Nb. Chondrite-normalized rare earth elements (REE) concentrations show a relative enrichment in light REE ($(La/Sm)_n = 1.48–1.73$) and an almost flat pattern for the heavy REEs ($(Dy/Yb)_n = 0.96–1.09$). The main-stage pumice does not show significant Eu* anomalies ($Eu^* = Eu/(Sm \times Gd)^{1/2} \sim 0.99$ to 1.12), whereas the late-stage pumice has the highest positive Eu* anomaly (1.16). Differences in moderately volatile trace elements between main-stage and late-stage pumices involve a higher V/Cu ratio in the late-stage pumice (~9 vs. 3–6) indicating a shift in oxidation state of the late-stage erupted magma.

Textural relations, mineralogy and mineral chemistry

The main-stage pumices are light gray to gray, with a porphyritic texture set in a vesicular, glass-rich, but microlite-bearing groundmass (Fig. 4a–j, Table 1). The phenocryst (crystals >100 mm) assemblage consists of Opx + Cpx + Plag + Mag + Amph and its pseudomorph (Amph*) ± olivine symplectite (Ol*) along with accessory apatite (Apa). The samples show a significant range of phenocryst content, from about 30 to 47 vol.%; plagioclase is the most abundant (< 14

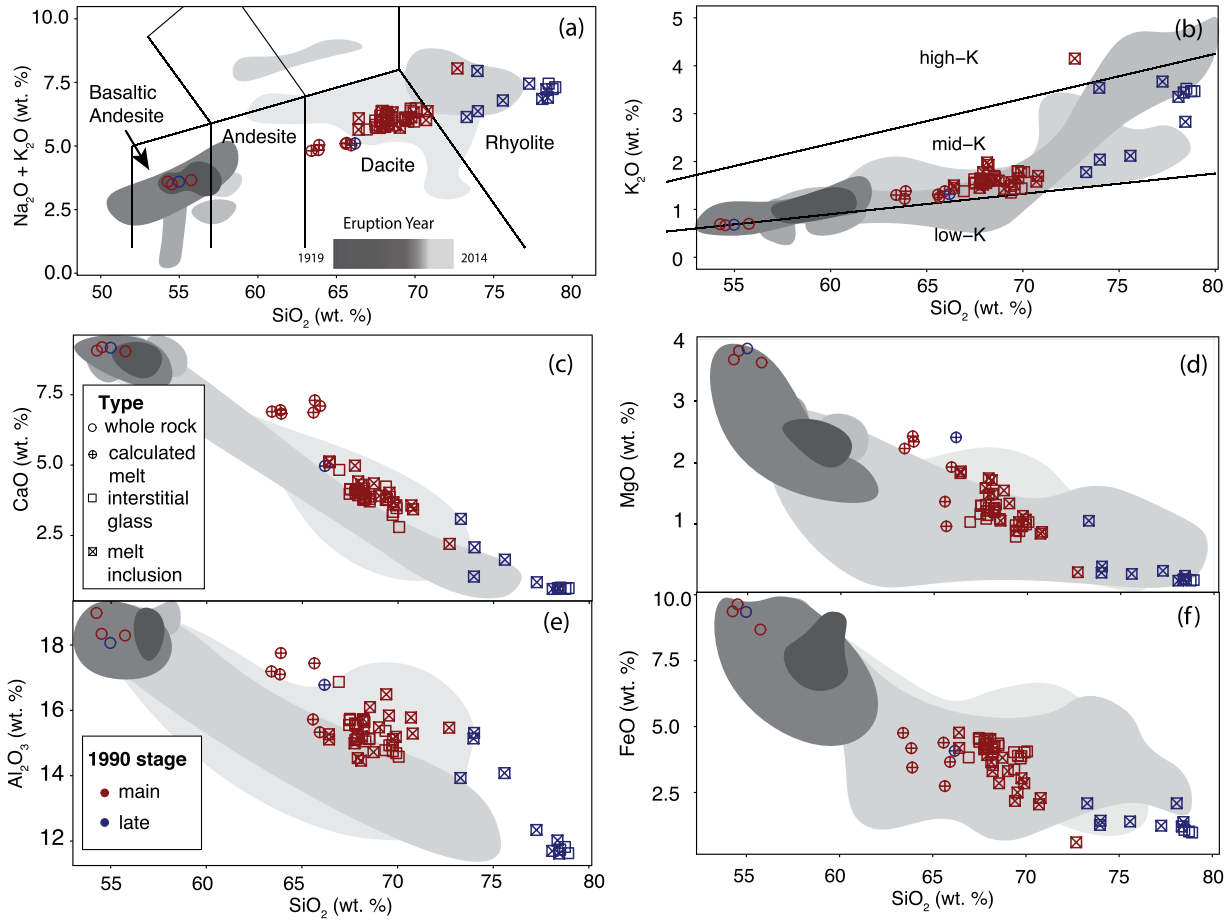

Fig. 3. Normalized major element oxide compositions (versus SiO_2) of whole rocks and glasses from the 1990 Kelud eruption analyzed in this study. (a) total alkali content ($Na_2O + K_2O$); (b) K_2O; (c) CaO; (d) MgO; (e) Al_2O_3; (f) FeO. Greyscale domains represent sample compositions from other eruptions of Kelud (1919—Sjarifudin & Claproth [1989], 1951—Sjarifudin and Claproth [1989], this study; 1966—this study; Pre-1990—Bernard [unpub. data]; 2007—Humaida [2013], Jeffery *et al.* [2013]; 2014—Cassidy *et al.* [2016], Goode [2018]). Although we acknowledge that there is an apparent correlation between the compositional domains from other Kelud eruptions, this trend is the result of combining whole rocks and glasses together. Whereas the whole rock is consistently basaltic andesite and completely overlaps for all eruptions, the different glass compositions are more evolved and thus form a trend within each respective eruption.

to 38 vol.%), followed by Opx (< 9 vol.%), Cpx (< 5 vol.%), Mag (< 5 vol.%), and Amph (< 0.2 vol.%). Phenocrysts of Plag, Opx or Cpx, are subhedral to euhedral or angular fragments of larger crystals.

Plag phenocrysts show a wide range of textures, including oscillatory zoning, sieved cores, and are typically broadly normally zoned with lower An at their rims than interiors (Fig. 4a). Unzoned Opx and Cpx phenocrysts (34% of the pyroxenes) are typically subhedral to euhedral and may host mineral and melt inclusions in their cores (Fig. 4b). Chemically zoned Opx phenocrysts (23% of the population) are typically reversely zoned, with a higher Mg-number rim mantling a rounded core (Fig. 4c). The compositional step from core to rim is sharp, even though some phenocrysts show more complex zoning at their rims (Fig. 4c). Normally zoned Opx phenocrysts (3%) are rare. Cpx phenocrysts are less commonly zoned; 18% show normal zoning in Mg-number, and about 1% reverse zoning (Fig. 4d). The cores of reversely zoned crystals are rounded or embayed, indicating a partial dissolution before rim regrowth. Mineral inclusions embedded in most phenocryst cores are commonly Fe-Ti oxides or apatite.

Glomerocrysts (13% of the total population) are made of Opx ± Cpx ± Plag ± Mag, with grain boundaries that can be rounded and sutured, or sub-rounded and partly exposed to the surrounding melt (Fig. 4f). We also found euhedral Cpx overgrowths over rounded and resorbed Opx phenocryst cores (3% of the total population), with inclusions of Mag outlining the core-overgrowths boundaries (Fig. 4g). Rare amphibole occurs as partially reacted phenocrysts (Fig. 4h). The pseudomorph reaction assemblage comprises anhedral fine-grained Cpx + Opx + Plag + Mag. Pseudomorphs after Amph breakdown consists of aggregates of Opx + Cpx + Plag + Mag in the original shape of the amphibole (Fig. 4i). Symplectites after olivine breakdown (Ol*, 1% of the total population) are made of Cpx + Opx + Mag (Fig. 4j). Microlites (< 100 mm) are mainly Plag, Cpx, Opx, Mag, and Apa, varying in habit from euhedral or skeletal to angular zoned fragments of larger crystals (Fig. 4e). Cpx microlites may have hourglass twinning, indicating rapid growth.

The late-stage pumices are light grey, with a porphyritic texture set in a vesicular and porous, glass-rich groundmass. They share the same rock-forming mineral assemblage as the main-stage pumices, but have higher phenocryst content (49 vol.%) and contain both quartz (Qz) and ilmenite. Opx, Cpx, and Plag phenocrysts can be

Table 1: Summary of sample description of 1990 samples used in our study. Asterisks (*) refer to the 1990 samples previously studied in Humaida (2013)

Sample ID	KELUT90B*	1990-PL1	1990-BR	90–2*	90–20*	90–23*	1990-PL2
Stage	Main	Main	Main	Main	Main	Main	Late
Latitude	−8.0	−7.9	−7.9	−7.9	−7.9	−7.9	−7.9
Longitude	112.0	112.3	112.3	112.3	112.3	112.3	112.3
Origin	Pumice fall	Pumice fall	Pumice flow	Pyroclastic flow*	Pyroclastic flow*	Pyroclastic flow*	Pumice fall
Hand specimen observations	light gray to gray porphyritic pumice	light gray to gray porphyritic pumice	light gray to gray porphyritic pumice	Thin section only	Thin section only	Thin section only	gray dense porphyritic pumice
Microscopic textures	Glomerocryst of plag + opx + cpx + mag. Overgrowth of cpx around rounded opx. Amph pseudomorphs and ol symplectites. Zoned and unzoned opx, cpx phenocrysts.	Glomerocryst of plag + opx + cpx + mag. Overgrowth of cpx around rounded opx. Contains partially reacted amph, amph pseudomorphs, and symplectite. Zoned and unzoned phenocrysts	Glomerocryst of plag + opx + cpx + mag. Overgrowth of cpx around rounded opx. Ol symplectite. Zoned and unzoned phenocrysts. Amph pseudomorph.	Glomerocryst of plag + opx + cpx + mag. Amph pseudomorph. Overgrowth of cpx around rounded opx. Sieve-textured plag.	Glomerocryst of plag + opx + cpx + mag. Sieve textured plag. Zoned and unzoned phenocrysts.	Glomerocryst of plag + opx + cpx + mag. Overgrowth of cpx around rounded opx. Ol symplectite. Zoned and unzoned phenocrysts	Glomerocryst of plag + opx + cpx + mag. Overgrowth of cpx around rounded opx. All phenocrysts are zoned. Large (>500um) amph pseudomorphs. Ol symplectite. Contains abundant qz bearing enclaves.
Matrix texture	vitric vesicular interstitial glass with variable vesicles. Rare microlites of plag + opx + cpx + mag	vitric vesicular interstitial glass with abundant fragments and microlites of (skeletal) plag + opx + cpx + mag. Opx microlites can be reversely zoned.	vitric vesicular interstitial glass with small vesicles. Rare microlites of plag + opx + cpx + mag	vitric vesicular interstitial glass	vitric vesicular interstitial glass	rare microlites of plag + opx + cpx + mag. Glass is partially devitrified.	vitric vesicular interstitial glass with thin, highly vesicular groundmass and thin (<10um) vesicle walls. Microlites consist of normally zoned plag.
Other observations			One of oikocryst of opx surrounding plag + mag				Qz is anhedral and interstitial, crystallizing around phenocrysts.
Zoning type							
Plag	oscillatory, normal rim normal, reverse, multiple	oscillatory, normal rim normal, reverse, multiple	oscillatory, normal rim normal, reverse, multiple	No observations	oscillatory, normal rim normal, reverse, multiple	oscillatory, normal rim normal, reverse, multiple	oscillatory, normal rim normal, reverse, multiple
Opx/Cpx				No observations			

Continued

Table 1: Continued

Sample ID	KELUT90B*	1990-PL1	1990-BR	90–2*	90–20*	90–23*	1990-PL2
Zoned Minerals	Plag, Opx, Cpx	Plag, Opx, Cpx	Plag, Opx, Cpx	Plag, Opx, Cpx	Plag, Opx, Cpx	Plag, Opx, Cpx	Plag, Opx, Cpx
Modal Mineralogy # **(vol.%)**							
Glass	57.6	69.1	68.3	59.5	66.9	52.8	50.7
Plag	29.8	14.1	22.4	30.4	19.6	37.6	31.4
Opx	4.6	6.6	2.4	3.8	4.6	3.3	8.7
Cpx	5.2	5.4	3.9	4.2	5.3	3.9	3.3
Mag	2.9	4.8	3.0	1.9	3.6	2.4	4.3
Amph	<0.1**	0.12	0.18**	0.12**			1.6**
Apa	< 0.1	< 0.1	< 0.1	< 0.1	< 0.1	< 0.1	< 0.1
Ol	< 0.1	< 0.1	< 0.1				< 0.1
Ilm							< 0.1
Total	100	100	100	100	100	100	98
Crystal Content for crystals > 1 mm (vol.%)	42.4	30.9	31.7	40.4	33.1	47.3	47.7
Analyses Conducted	XRF, SEM (WDS/EDS), EPMA	XRF, SEM (WDS/EDS), EPMA	XRF, SEM (WDS), EPMA	SEM (WDS)	SEM (WDS)	XRF, SEM (WDS/EDS), EPMA	XRF, SEM (WDS/EDS), EPMA

#Plag = plagioclase; Opx = orthopyroxene; Cpx = clinopyroxene; Mag = magnetite; Amph = amphibole; Apa = apatite; Ol = olivine; Ilm = ilmenite

*Samples from H. Humaida's unpublished doctoral thesis (Humaida, 2013)

**Amph is pseudomorph

***Ol has been turned to symplectite

Table 2: Major and trace element composition for 1990 whole rocks. KELUT90B was used as input for rhyolite-MELTS modeling

Sample ID	KELUT-90B	KELUD-1990-PL1	KELUD-1990-BR	KELUD-1990-PL2
Stage	Main	Main	Main	Late
Major elements (wt.%)				
SiO_2	56.15	54.17	54.6	54.42
Al_2O_3	18.42	18.95	18.36	17.88
FeO*	8.74	9.35	9.65	9.26
MnO	0.2	0.2	0.21	0.2
MgO	3.65	3.66	3.81	3.81
CaO	9.1	9.05	9.2	9.08
Na_2O	2.99	2.9	2.82	2.89
K_2O	0.7	0.69	0.67	0.67
TiO_2	0.64	0.69	0.67	0.65
P_2O_5	0.13	0.16	0.14	0.13
Total	100.7	99.8	100.4	99.0
Trace elements (mg/kg)				
La	5.82	6.05	6.0	5.96
Ce	13.2	13.5	13.3	13.3
Pr	1.82	1.76	1.74	1.78
Nd	8.34	8.34	8.01	8.23
Sm	2.55	2.37	2.24	2.36
Eu	0.873	0.854	0.817	0.902
Gd	2.84	2.32	2.52	2.4
Tb	0.46	0.44	0.43	0.41
Dy	2.72	2.78	2.60	2.74
Ho	0.55	0.56	0.53	0.58
Er	1.72	1.67	1.64	1.7
Tm	0.287	0.251	0.248	0.256
Yb	1.89	1.71	1.71	1.7
Lu	0.29	0.27	0.25	0.27
Y	15.7	15.3	15.6	15.3
Zr	44	39	38	38
Nb	1.2	0.9	0.8	0.9
Hf	1.5	1.1	1.1	1.2
Ta	0.11	0.04	0.02	0.05
Th	0.93	0.86	0.83	0.85
U	0.38	0.34	0.33	0.35
Rb	13	12	12	12
Cs	1.0	0.8	0.8	0.8
Sr	577	605	580	575
Ba	484	479	463	465
Sc	20	19	20	19
V	183	179	180	179
Cr	30	< 20	< 20	80
Co	19	19	20	20
Cu	40	60	30	20
Pb	9	8	8	8
Zn	60	60	70	60
Sn	4	3	< 1	1
W	1.9	2.3	2.5	0.5
Ga	16	15	16	16
Ge	1.4	1.3	1.3	1.3
Tl	0.49	< 0.05	< 0.05	< 0.05
Sb	0.8	< 0.2	0.3	0.4
Eu*	0.99	1.12	1.05	1.16

Continued

Table 2: Continued

Sample ID	KELUT-90B	KELUD-1990-PL1	KELUD-1990-BR	KELUD-1990-PL2
CI Chondrite normalized REE				
$(La/Yb)_n$	2.21	2.54	2.52	2.52
$(La/Sm)_n$	1.48	1.65	1.73	1.63
$(Dy/Yb)_n$	0.96	1.09	1.02	1.08
V/Cu	4.58	2.98	6.00	8.95

Eu* = Eu / (Sm × Gd)1/2, with all compositions are normalized to primitive mantle.
FeO* = total iron oxide, converted to Fe2+
See data on glass inclusions and calculated matrix in supplementary data.

chemically zoned. Plagioclase shows progressive, normally zoned rims (Fig. 5a). Opx phenocrysts are typically normally zoned (44% of the total) rather than reversely zoned (2%) (Fig. 5b). Phenocryst edges are serrated or show reaction rims, likely from partial melting of evolved interstitial glass. Glomerocrysts are common (39% of the total population surveyed in this study) and with the same mineralogy as those in the main-stage pumices (Fig. 5c). Cpx can be found as overgrowths on Opx (5%) and are more abundant than in main-stage pumices (Fig. 5d). The groundmass is highly porous with thin vesicle walls (< 10 mm) and rhyolitic interstitial glass (Fig. 5e). Microlites are mainly Plag plus some Cpx, Opx, Mag, and Apa (Fig. 5f). Fe-Ti oxides are Mag and Ilm, with Mag partially surrounded by frayed Ilm rims wherever Mag edges are exposed to melt (Fig. 5g). Quartz crystals commonly fill the interstices surrounding phenocrysts of Plag ± Opx ± Cpx ± Mag in enclaves, indicating that the magma cooled enough to evolve to high SiO_2 content and crystallize Qz (Fig. 5h). Amphibole is completely reacted to pseudomorphs (7%) that are considerably larger than the main-stage pseudomorph (> 500 mm) and appear as fine-grained Cpx + Opx + Plag + Mag assemblages in the shape of the original Amph crystal (Fig. 5i). Olivine symplectites (2% of the total population) are similar in morphology and mineralogy to those in main-stage pumices (Fig. 5j).

Mineral compositions and traverses

The main-stage Plag ranges from An = 58 to 90 (Fig. 6a, Table 3), with cores showing a bimodal distribution at $An_{58–75}$ and $An_{75–90}$, whereas rims are mainly unimodal at $An_{58–75}$. Plagioclase phenocrysts can be classified into two main textural types (Fig 6): Type 1a Plag has a spongy, sieved core (~ An_{86}) mantled by a zone at An = 70–90, which is in turn surrounded by a lower-An rim (58–70), some crystals can also have an intermediate sieved zone, which we call Type 1b. Type 2 crystals do not show significant zoning or textures aside from oscillatory zoning, with cores fluctuating between $An_{60–75}$ and $An_{75–90}$ and surrounded by lower An rim ($An_{60–70}$) (Fig. 6d). Plagioclase microlites are zoned, with cores of $An_{60–85}$ mantled by rims of $An_{60–62}$ that are similar to Type 2 Plag phenocrysts. Compositional profiles in Type 1b crystals show one plateau that coincides with a light grey zone in BSE images (An_{80}) and darker rim (An_{60}). The outer zones of these crystals show multiple compositional fluctuations, from about An 62 to 75 (Fig. 6e–f). We have few Plag analyses from the late-stage pumice. These have similar phenocryst types and compositions as the main-stage pumices, but a major difference is the presence of a more evolved rim population at about An_{40}. Such a low-An rim population is consistent with the more evolved compositions of the interstitial melt in late-stage pumice.

Main-stage Opx phenocrysts display a bimodal distribution with a mode at Mg-number = 62–70 and another one at 70–74 (Fig. 7a, Table 4). The low Mg-number mode characterizes glomerocrysts, Opx cores with Cpx overgrowths, and most cores of both zoned and unzoned phenocryst. A Mg-number > 70 is common for rims of reversely zoned phenocrysts and microlites. Reversely zoned Opx phenocrysts (Fig. 7b) commonly display sharp compositional steps, with higher Mg-number in rims (72–74) than cores (66–70) (Fig. 7c). Opx crystals in late-stage pumice show a wide compositional spread (Mg-number = 58–72), and many are more evolved than Opx from the main-stage (Table 4). Most unzoned crystals have a core compositionally similar to main-stage Opx (Mg-number = 68–69), and some Opx phenocrysts show normal zoning (Fig 7d), with Mg-number 64–68 in cores and 58–62 in rims (Fig. 7e). The composition of Opx in glomerocrysts (Mg-number = 59–72) overlap with those of phenocryst cores and microlites. Overgrowth Opx cores have similar compositions to main-stage overgrowth ones (Mg-number = 68–70). Opx in Amph breakdown textures overlap with most other compositions (Mg-number = 60–68).

Cpx phenocrysts in main-stage samples (Mg-number = 70–78, $Wo_{38–45}En_{40–48}$) show a narrower compositional range than Opx, and vary depending on the textural group (Fig. 8a and Table 4; for Wo and En distributions, see Fig. S3). Phenocryst cores either overlap or have lower Mg-number (70–76) than rims (72–76), rarely Cpx also show reverse zoning (Fig. 8b–c). Glomerocryst Cpx cores overlap with phenocryst cores at Mg-number = 71–76. Cpx overgrowth and microlites record the largest compositional range in Mg-number (72–74), and in Wo and En content ($Wo_{41–44}En_{40–43}$) compared to the rest of the Cpx. Late-stage Cpx (Mg-number = 58–73, $Wo_{38–48}En_{31–48}$; Table 4), are more evolved than main-stage Cpx. Phenocrysts show normal zoning (Fig. 8d), with higher Mg-number in cores (= 70–76) than rims (= 68–70; Fig. 8e). Cpx in glomerocrysts display the widest compositional range (Mg-number = 62 to 79, $Wo_{41–49}En_{32–45}$). Cpx microlites and overgrowth (Mg-number = 72–74, $Wo_{42–44}En_{41–43}$) have higher Mg and Ca compared to the phenocrysts. Cpx found as pseudomorph (Mg-number = 69–74, $Wo_{41–44}En_{39–42}$) is likely produced from Amph breakdown.

The two partially reacted amphibole phenocrysts (Mg-number = 76–83) from the main-stage straddle the magnesio-hastingsite and tschermakite-pargasite end-members (Table 5) defined by Leake *et al.* (1997). Both phenocrysts have reaction rims consisting of an anhedral, fine-grained assemblage of Opx + Cpx + Plag +

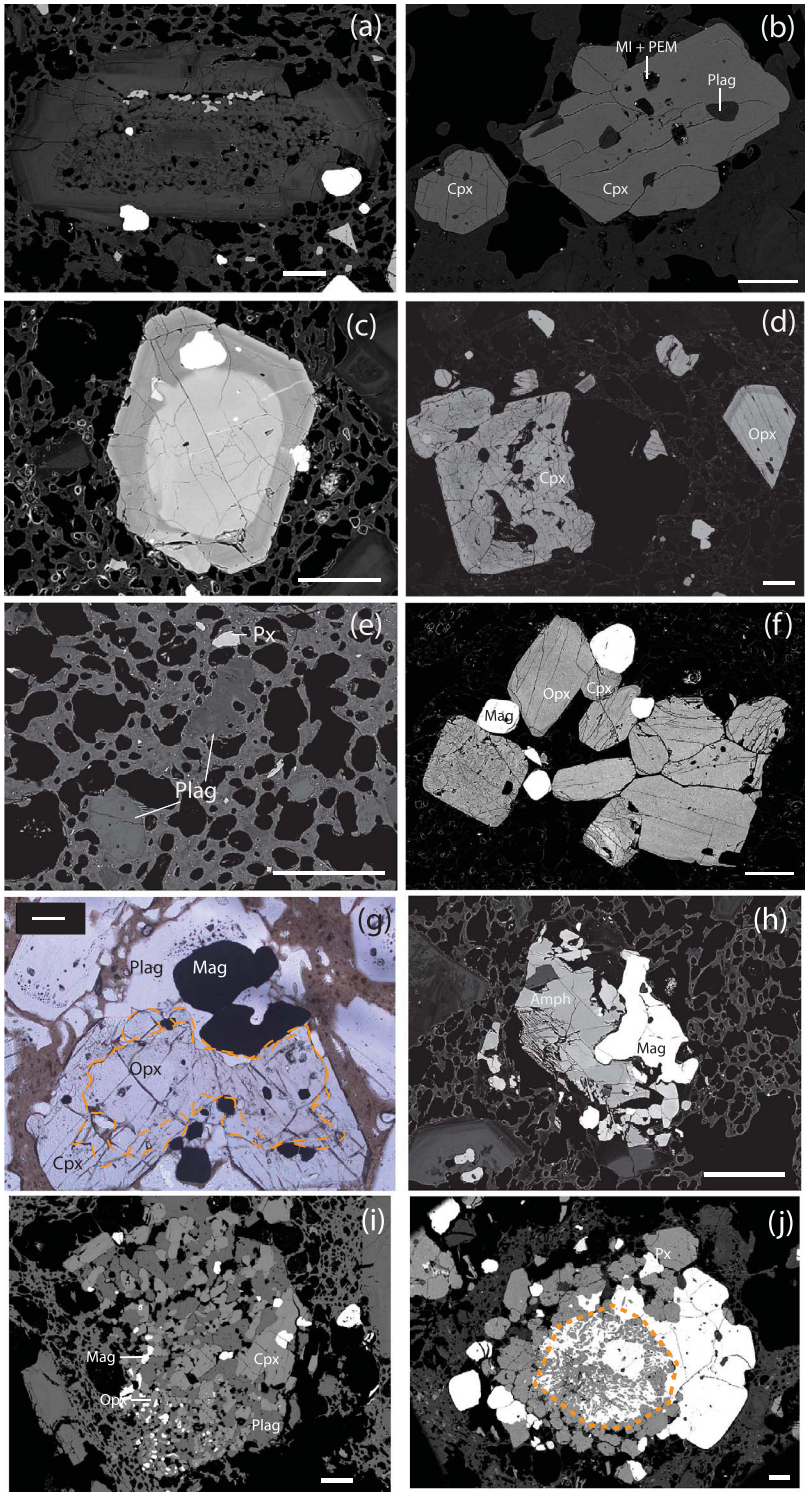

Fig. 4. Plane-polarized (PPL) and BSE images of representative mineral textures pumices from the main eruptive stage. (a) Type 2 Plag phenocryst with a partially resorbed core mantled by a spongy-sieve textured growth zone with a normally-zoned rim. Light grey inclusions are apatite (Apa). (b) Cpx phenocryst with glassy inclusions (MI), Plag inclusions, and post-entrapment daughter minerals (PEM). (c) Euhedral reversely zoned Opx phenocryst with Apa and Mag inclusions. (d) Normally zoned Cpx and reversely zoned Opx. The normally zoned Cpx hosts many irregular melt inclusions. (e) Groundmass texture with plagioclase and pyroxene microlites surrounded by quenched interstitial glass. (f) Glomerocryst of Opx + Cpx + Mag showing both unsutured and sutured grain boundaries. (g) PPL image of Cpx overgrowth mantling rounded Opx core with Mag phenocrysts along boundaries. Orange dashed line shows the Opx-Cpx boundary (h) Partially reacted Amph grains with anhedral Mag phenocrysts attached. (i) Pseudomorph after Amph breakdown, filled with fine-grained assemblage of Opx + Cpx + Plag + Mag. (j) Symplectitic texture after olivine breakdown showing anhedral pyroxenes surrounded by stringy magnetite.

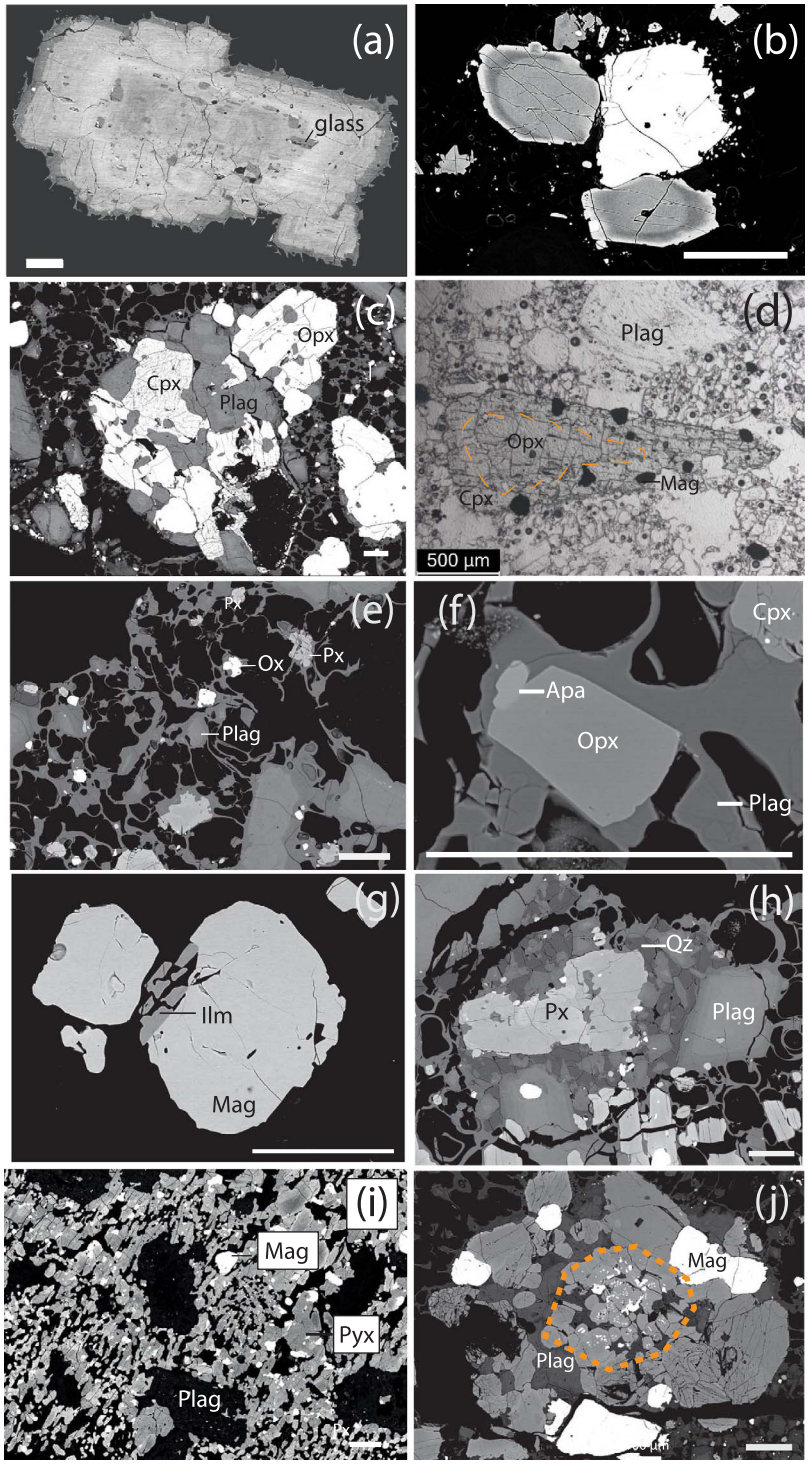

Fig. 5. PPL and BSE images of representative mineral textures in the pumice from the late eruption stage. White and grey scale bars indicate 100 □m scale. (a) Normally zoned Plag phenocryst with glassy inclusions. (b) Multiply zoned Opx phenocrysts attached to partially reacted Mag glomerocryst, featuring reverse mantling growth zone followed by normal rim. (c) Glomerocryst comprising anhedral to subhedral Opx + Cpx + Plag + Mag. (d) PPL image of Cpx overgrowth mantling rounded Opx core. Orange dashed line marks the Opx-Cpx boundary. (e) Groundmass textures with Fe-Ti oxides, pyroxenes, and Plag microlites. (f) Magnified view of Opx + Apa + Plag + Cpx microlites; (g) Mag phenocryst with Ilm rims. (h) Quartz bearing enclaves, where Qz forms an interstitial phase around the pyroxene and plagioclase phenocrysts. (i) Pseudomorph of Amph, with Plag inclusions. (j) Symplectitic texture surrounded by Mag, Plag, and pyroxene phenocrysts.

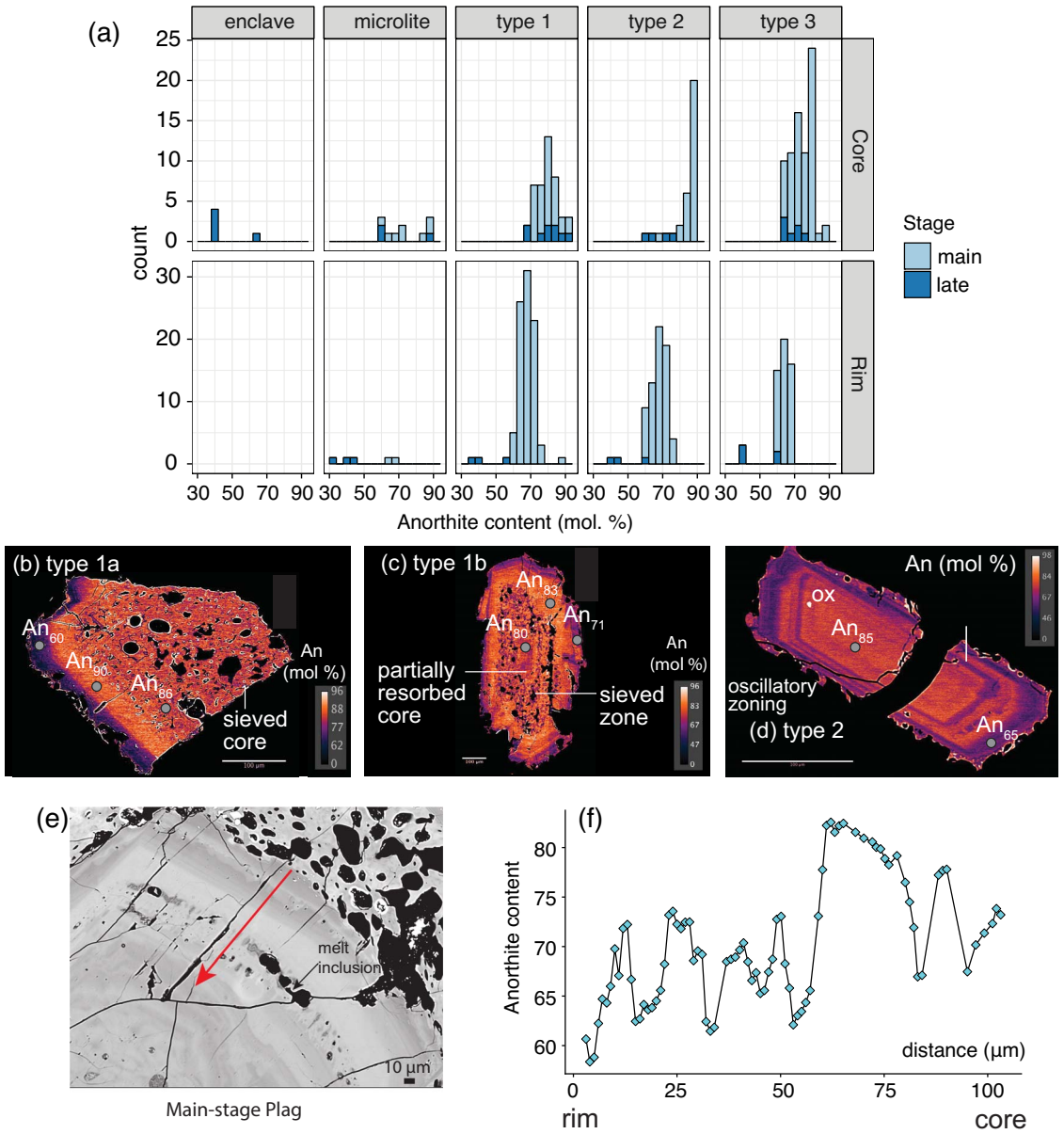

Fig. 6. (a) False color BSE images, histograms and representative traverses of plagioclase compositions from the main and late eruption stage, further divided into type 1–3 phenocrysts, microlites, and enclaves. (b) Annotated false color BSE image of a type 1 Plag, with An compositions from spot analyses. (c) Same for type 2 Plag, with An compositions from spot analyses. (d) Same for type 3 Plag, with An compositions from spot analyses. (e) Annotated BSE image of a main stage Plag with the analyzed traverse from rim to core shown by a red arrow. (f) Traverse analysis of An content from rim to core, denoted by the red arrow.

Mag. Magnetite in main-stage samples shows a narrow range of $X_{usp} = 0.28–0.30$ (Table 5), whereas magnetite in late-stage pumice shows a bimodal distribution at about 0.30 and at 0.31–0.34 (Fig. S4a), with no overlap. Ilmenite also displays a bimodal distribution, with a first mode at $X_{ilm} = 0.88–0.91$ and a second one $X_{ilm} = 0.91–0.92$ (Fig. S4b).

Pre-eruptive magma storage conditions

Pyroxene temperature constraints

The pyroxene-melt equilibrium temperatures from the main-eruptive stage samples show a wide range, from about 950 to 1100°C across textural groups. Opx-melt temperatures vary between about 980 to 1050°C, and the crystal core temperatures overlap or are somewhat higher than those obtained from the rims. The high temperature range from Opx-melt equilibria is close to or overlaps with the whole-rock liquidus temperatures ($T_{liquidus}$) calculated with MELTS at NNO with 3–4 wt.% of water in the melt, and about 50°C lower the liquidus with 2 wt.% water in the melt (Fig. 9a). Moreover, temperatures recorded from individual core to rim crystal traverses record a temperature decrease of about <50°C, even for crystals that are reversely zoned in Mg-number (Fig. S5). Opx microlite-melt temperatures overlap with those of the phenocryst rims. Cpx-melt temperatures overlap or a somewhat higher than those of Opx, with a mode at ~1050°C. The temperatures of crystal cores and rims overlap, except for reversely zoned (in Mg-number) Cpx traverses,

Table 3: Plagioclase compositions and textures in pumices representative for the main- and late-stage eruption stages

	KELUT90B-PLG-b1	KELUT90B-PLG-b2	KELUT90B-PLG-y4	KELUT90B-PLG-r5	PL1-plag3-row3	PL1-plag3-row5-rim	PL2–2-plag4	PL2–2-plag1	PL2–2-plag3	PL2-plag3	PL2-plag-encl1	PL2-plag1	PL2-plag3
Stage	Plag	Plag	Plag	Plag	Plag	Plag	Plag	Plag	Plag	Plag	Plag	Plag	Plag
	Main	Main	Main	Main	Main	Main	Late	Late	Late	Late	Late	Late	Late
	Type 1 core	Type 2 core	Type 3 core	Rim	Microlite - core	Microlite - rim	Type 1 core	Type 2 core	Type 3 core	Rim	Enclave	Microlite - core	Microlite - rim
wt.%													
SiO_2	48.7	46.5	49.2	52.4	49.9	51.3	46.0	47.9	48.6	57.5	57.8	51.7	57.5
Al_2O_3	31.5	33.2	30.9	29.4	31.6	30.7	33.6	31.6	31.6	26.1	26.4	30.4	26.1
Na_2O	2.2	1.4	2.5	3.7	3.2	3.8	2.0	3.4	3.6	6.8	6.9	4.0	6.8
CaO	15.6	17.3	15.1	13.5	15.0	14.0	17.0	15.0	14.6	8.0	9.0	13.0	8.0
K_2O	0.0	0.0	0.1	0.1	0.1	0.1	0.1	0.1	0.1	0.3	0.3	0.1	0.3
MgO	NA	NA	NA	NA	0.0	0.1	0.0	0.0	0.0	0.0	0.0	0.1	0.0
FeO	0.6	0.6	0.6	0.7	0.6	0.6	0.3	0.3	0.3	0.5	0.6	0.5	0.5
Total	98.6	98.9	98.4	99.8	100.5	100.6	98.9	98.3	98.8	99.2	101.0	99.8	99.2
An	79.8	87.2	76.9	66.9	71.5	66.3	82.5	71.1	69.2	40.8	40.6	64.7	40.8

An = 100 × Ca/(Ca + Na). See supplementary materials for more analyses.
NA = not available

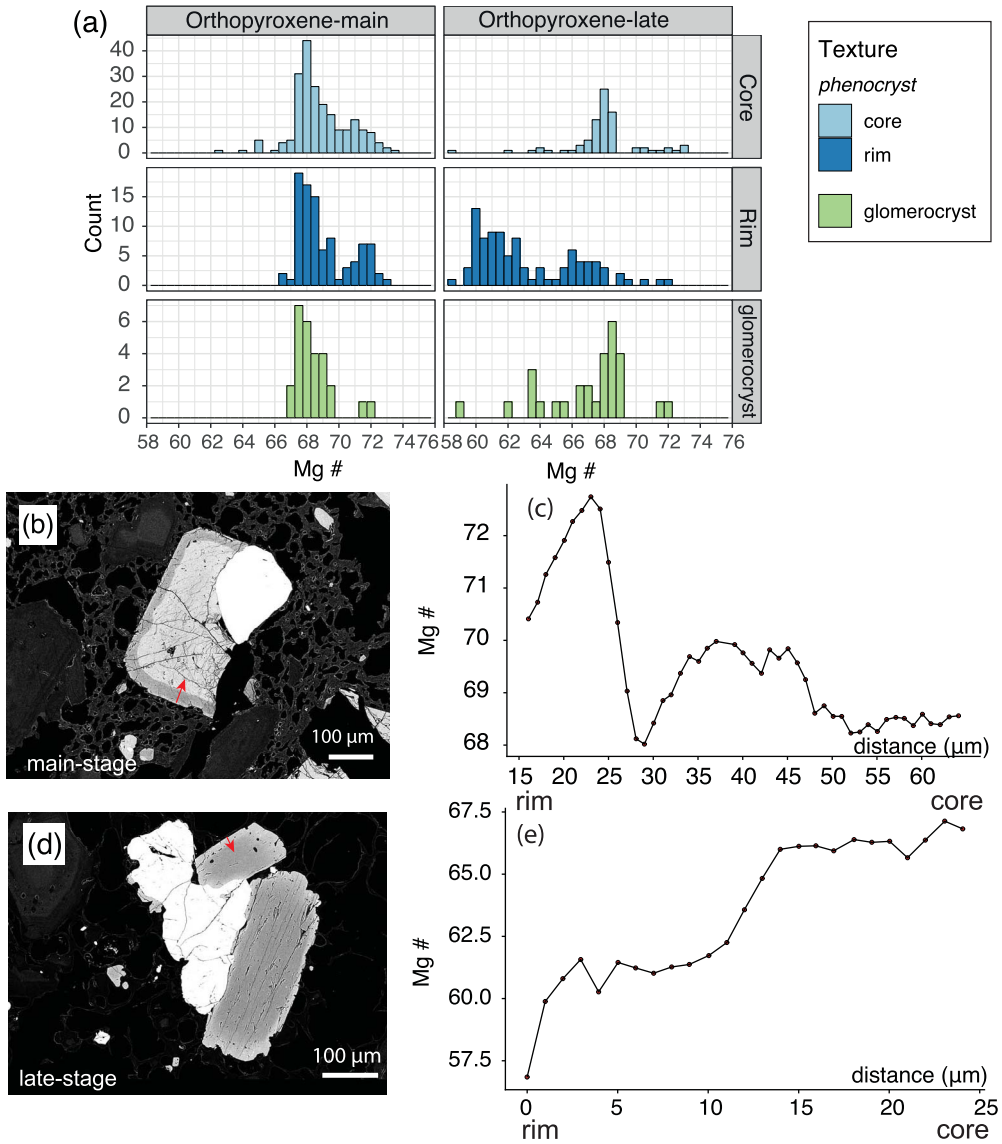

Fig. 7. (a) Histograms and representative traverses of Opx compositions, subdivided according to the textural groups: cores of phenocrysts, overgrowth Opx cores and microlites; rims of zoned phenocrysts; and glomerocrysts. Red arrows indicate the direction of traverse analysis. (b) BSE image of a reversely zoned main-stage Opx. (c) Traverse analyses from rim to core of Mg-number of a main-stage Opx. (d) BSE image of a normally zoned late-stage Opx. (e) Traverse analysis from rim to core of Mg-number of a late-stage Opx.

where core temperatures are generally higher than the rims. Despite this apparent core to rim temperature decrease, the crystal cores in zoned Opx and Cpx are resorbed, and suggest a period of crystal dissolution between cores and rims induced by temperature and compositional effects. Finally, Opx-Cpx temperatures partly overlap or are slightly higher than those of Opx and Cpx-melt with one main mode at ~1000 (± 25°C) and smaller one at ~1080 (± 25°C). Temperature ranges from core–core pairs, rim–rim pairs, and microlites overlap.

Opx and Cpx core-melt temperatures for the late-stage deposits are similar and overlap with those of the main-stage (1040–1070°C), and are somewhat higher than those of the rims and microlites (970–1020°C) (Fig. 9a). The cores of zoned Opx and Cpx crystals tend also to be resorbed as in the main-stage samples. Opx-Cpx pair temperatures (990–1030°C) overlap between core and rims (Figure 9). Opx-Cpx temperatures for the microlites in late-stage pumice overlap with those for crystal rims but are lower than those inferred for Opx-Cpx pairs in main-stage pumice.

Magnetite-ilmenite oxybarometer

Temperatures obtained from Mag-Ilm pairs from the late-stage pumice are 780–850°C, i.e. 100 to 150°C lower than those inferred from silicate minerals (Fig. 9a). Temperatures obtained using the Ghiorso and Evans (2008) model have a mode at 825°C, and an fO_2 of about 0.5–2 log units above the NNO buffer. The model of Sauerzapf *et al.* (2008) model yields somewhat lower temperatures (T = 780–800°C), but a similar range in fO_2. Such low temperatures indicate that the late-stage magmas experienced at some point in their history cooler storage conditions than the main-stage magma, which is consistent with their higher crystallinity, and the presence of low temperature minerals such as quartz.

Table 4: Opx and Cpx compositions and textures in pumices representative for the main and late eruption stages

	PL1–1-px-z1a	PL1–1-px-MX1	90B-opxcpx17	PL1-site1-px4	PX6-c-only	glom1-c-only	PL2–2px7	PL2-site1-px7	PL1–1-px6	90–23-px18	90B-opxcorecpxrim-1	PL1-site1-px8	PX5-core-only	glom4-c-only	PL2-px7	PL2-site1-px2
	Opx	Opx	Opx	Opx	Opx	Opx	Opx	Opx	Cpx	Cpx	Cpx	Cpx	Cpx	Cpx	Cpx	Cpx
	Main	Main	Main	Main	Late	Late	Late	Late	Main	Main	Main	Main	Late	Late	Late	Late
	Pheno	Glom	Over-growth	Microlite	Pheno	Glom	Over-growth	Microlite	Pheno	Glom	Over-growth	Microlite	Pheno	Glom	Over-growth	Microlite
wt.%																
SiO_2	53.36	52.02	52.1	52.2	53.09	52.43	53.1	51.3	52.48	51.8	50.81	51.23	51.4	51.7	51.4	51.0
TiO_2	0.18	0.21	0.2	0.2	0.12	0.18	0.1	0.2	0.33	0.4	0.32	0.37	0.3	0.4	0.4	0.3
Al_2O_3	1.07	1.75	1.4	1.8	1.01	1.61	0.8	1.6	1.71	2.0	1.82	1.59	2.0	2.2	1.7	1.6
FeO*	21.51	21.90	20.1	18.9	18.87	19.32	18.5	21.2	10.85	11.0	9.84	10.06	9.4	9.5	9.4	11.2
MnO	0.85	0.71	0.9	0.7	0.73	0.71	0.7	0.7	0.52	0.4	0.48	0.48	0.4	0.4	0.4	0.5
MgO	23.23	23.39	23.4	24.5	23.07	22.74	23.6	22.9	14.57	14.7	14.53	14.73	14.6	14.3	14.3	14.4
CaO	1.42	1.34	1.2	1.5	1.57	1.56	1.5	1.6	20.75	19.4	20.67	20.27	21.0	20.9	21.2	20.0
Na_2O	0.01	0.01	0.0	0.1	0.02	0.02	0.0	0.2	0.3	0.3	0.29	1.38	0.3	0.3	0.3	1.8
Total Oxide	101.60	101.30	99.2	99.9	98.50	98.60	98.4	99.7	101.5	99.9	98.8	100.1	99.5	99.7	99.1	100.9
Mg Number	65.81	65.6	67.5	69.8	68.5	67.7	69.4	65.8	70.5	70.4	72.5	72.3	73.4	72.9	73.0	71.8
Wo	2.81	2.63	2.4	2.9	3.24	3.23	3.1	3.1	41.9	40.1	42.59	41.7	43.2	43.4	43.8	41.8
En	63.96	63.84	65.8	67.7	66.32	65.53	67.2	63.7	41.0	42.2	41.57	42.2	41.7	41.3	41.1	41.8
Fs	33.23	33.53	31.7	29.3	30.43	31.23	29.7	33.1	17.1	17.8	15.84	16.2	15.1	15.3	15.2	16.4

FeO* and structural end-members based on Deer et al. (1992). Mg Number = Mg/(Mg + Fetotal). Please see supplementary material for more analyses.

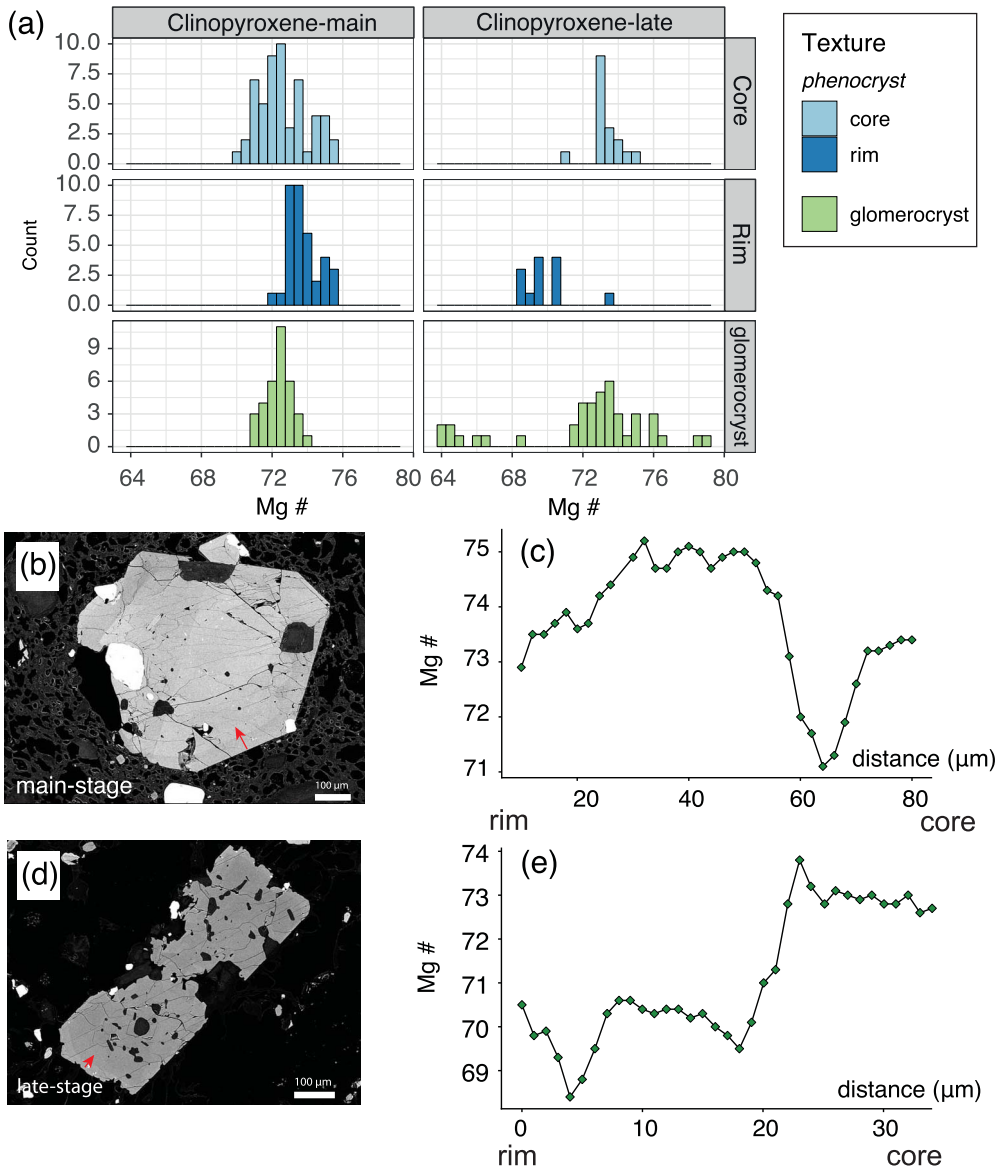

Fig. 8. (a) Histograms and representative traverses of Cpx compositions, subdivided into the same textural groups as Opx. Traverse directions shown by red arrows. (b) BSE image of a reversely zoned main-stage Cpx. (c) Traverse from rim to core of Mg-number of a main-stage Cpx. (d) BSE image of a normally-zoned late-stage Cpx. (e) Traverse analysis from rim to core of Mg-number of a late-stage Cpx.

Amphibole-melt geothermobarometer

We obtained temperature and pressure estimates from the two Amph phenocrysts from the main-stage samples (Fig. 10). The Putirka (2016) and Li *et al.* (2021) combined formulation yields 960–980°C, and 400–550 MPa. Slightly lower temperatures (920–970°C) but higher pressures (480–590 MPa) are derived from the Ridolfi & Renzulli (2012) Amph-only formulation, whereas significantly higher temperatures (1000–1030°C) and pressures (570–830 MPa) result when applying the formulation of Ridolfi *et al.* (2010). These temperature estimates for amphibole either overlap with or are lower than pyroxene-based temperatures for crystal rims and microlites.

Clinopyroxene-melt geobarometer

We obtained pressure estimates from the Cpx-melt pairs from the main-stage samples using the formulations by Neave and Putirka (2017) and Putirka (2008) (Fig. S10). Both formulations yield overlapping pressures of 100–350 MPa, with comparable peaks at ~150 MPa. These pressure estimates overlap with saturation pressure estimates, but are lower than estimates from Amph based geobarometers.

Dissolved water content, saturation pressures, and exsolved fluids

We assessed the concentration of dissolved water in the melt with the plagioclase-melt equilibrium model of Waters & Lange (2015), using the Plag rim and interstitial glass compositions, and the temperature obtained from Opx rim-melt (Table S3). Main-stage plagioclase rims of $An_{60–70}$ yield ~2–4 wt.% water in the melt, consistent with the water content required to crystallize amphibole. In comparison, the late-stage plagioclase rims have lower anorthite content, with An_{40} that gave higher values of ~4–6 wt.% water in the melt. Cassidy *et al.*

Table 5: Representative Amph and Fe-Ti oxides compositions in main- and late-stage pumices

	KELUD1990-PL1new-1-amph2	KELUD1990PL1_amph1_8		90–23-Mag1	Mag-Ilm-13	Mag-Ilm-26
	Amph	Amph		Mag	Mag	Ilm
	Main	Main		Main	Late	Late
SiO_2	41.46	42.59	TiO_2	8.7	9.4	43.9
TiO_2	1.41	1.55	Al_2O_3	2.9	1.2	2.4
Al_2O_3	14.92	14.01	Cr_2O_3	0.0	0.1	0.0
Cr_2O_3	0.00	0.02	FeO	39.6	41.2	34.2
Fe_2O_3	5.10	8.61	Fe_2O_3	44.7	44.3	14.6
FeO	7.04	3.45	MnO	0.5	0.6	1.0
MnO	0.15	0.17	MgO	2.1	1.0	2.3
MgO	13.28	14.35		0.11	0.1	0.1
CaO	12.50	11.68				
Na_2O	2.29	2.25	Total	99.0	97.9	98.68
K_2O	0.31	0.29				
F		0.165	Structural cations***			
Cl			Ti	1.70	2.0	6.9
H_2O_{calc}	1.93	1.87	Al	0.89	0.4	0.3
Total	100.39	101.01	Cr	0.01	0.0	0.0
			Fe^{2+}	12.44	13.1	7.4
Structural Formula			Fe^{3+}	3.19	3.0	0.9
T site			Mn	0.11	0.1	0.2
Si	6.00	6.07	Mg	0.81	0.4	0.7
Al^{IV}	2.00	1.93	Si	0.03	0.0	0.0
Ti	0.0	0.00				
Al^{VI}	0.55	0.43				
Ti	0.15	0.17				
Cr	0.00	0.00				
Fe^{3+}	0.56	0.92				
Mg	2.87	3.05				
Fe^{2+}	0.85	0.41				
Mn	0.02	0.02				
B site						
Fe^{2+}	0.00	0.00				
Ca	1.94	1.78				
Na	0.06	0.22				
A site						
Na	0.58	0.41				
K	0.06	0.05				
$Mg/(Mg + Fe^{2+})$	0.84	0.88				
Mg Number	78.02	76.75				
P (MPa)*	508	484				
T (°C)*	912	939				
End-member**	Magnesio-Hastingsite	Tschermakite-Pargasite				

*Pressure and temperature calculated using formulation of Ridolfi & Renzulli (2012)
**Structural formulae according to Leake *et al.* (1997)
***Structural cations calculated using Droop (1987)

(2016) studied the 2014 eruption deposits and found that plagioclase-hosted melt inclusions contained 0.4–2.3 wt.% water and up to 336 mg/kg CO_2. Assuming that this CO_2 content is also representative of the 1990 melts, we calculated volatile saturation pressures for the main-stage pumices of 110 to 170 MPa (~4–7 km depth), whereas for the late-stage pumices we obtained 150 to 230 MPa (~6–9 km depth) (Fig. 11; Table S3). The whole-rock, pre-eruptive temperature, mineral assemblage, and phenocryst content of the 1990

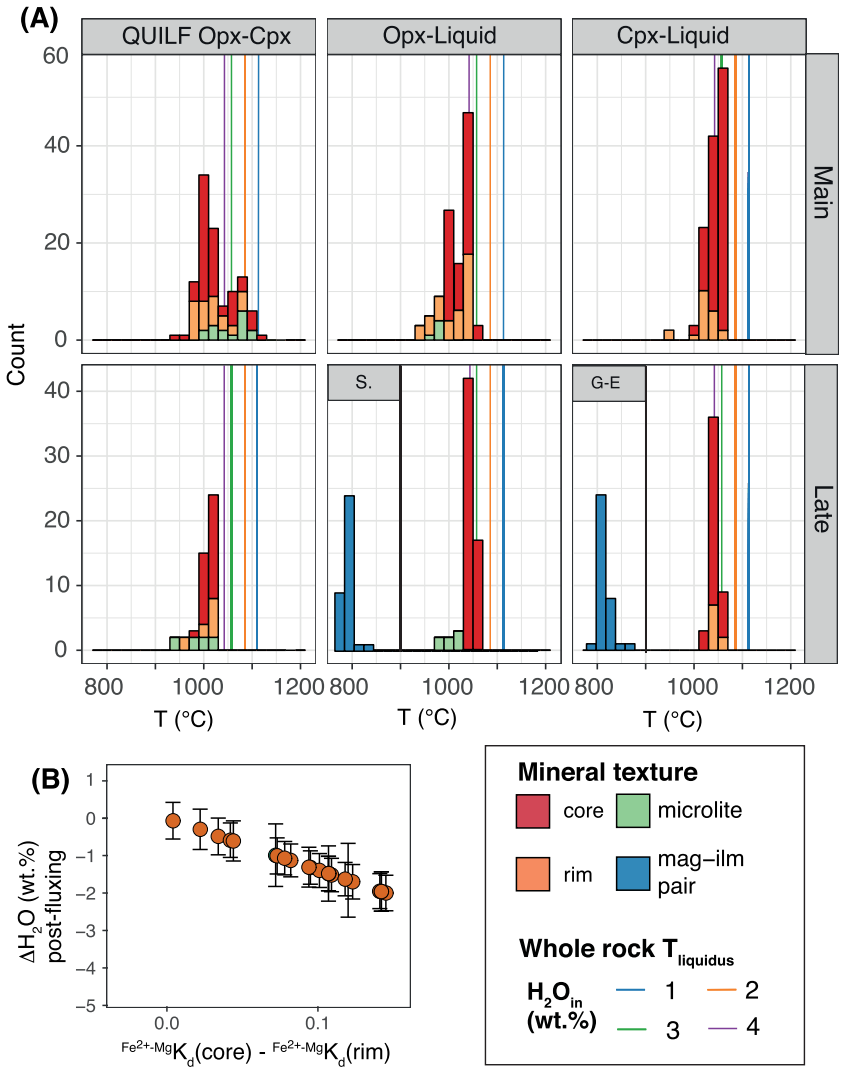

Fig. 9. (a) Histograms of calculated temperatures for the main- and late-stage pumice samples constrained by different geothermometers and for various textures (cores, rims, microlites, Mag-Ilm pairs). Geothermometers include: two-pyroxene QUIIF geothermometer (Andersen *et al.*, 1993); Opx- and Cpx-melt geothermometers (eq. 28a and eq. 33, respectively) (Putirka 2008), using core-whole rock pairs and rim-interstitial glass pairs; and Mag-Ilm geothermometer for late-stage pumice (GE: Ghiorso & Evans [2008]; S: Sauerzapf *et al.* [2008]). Whole rock liquidus temperatures ($T_{liquidus}$) at various water contents are also provided for comparison and were calculated using rhyolite-MELTS (Gualda *et al.*, 2012; Ghiorso & Gualda, 2015) and the main-stage pumice KELUT90B used as input material. (b): $D^{Mg\text{-}Fe2+}K_d$ vs. DH_2O, as recorded by main-stage Opx cores and rims calculated using an empirical relationship from experimental results by Waters & Lange (2017).

main pumices and the 2014 pumice are similar and thus suggest that they had similar pre-eruptive content (Utami *et al.*, in preparation).

We also assessed the existence of an exsolved pre-eruptive volatile phase by comparing the SO_2 mass that was degassed during the eruption as measured by satellite data (e.g. Carn 2019), and that which can be produced by degassing of the melt alone (e.g. by the petrologic method, see methods section above). We used the total SO_2 gas detected by satellite over the course of the eruption from February to March 1990 (~0.17 Mt of SO_2; Carn *et al.* 2015). After correcting for post-entrapment crystallization, pyroxene-hosted melt inclusions have 440–1110 mg/kg SO_2 (Table 8) whereas the interstitial melt has about 60–90 SO_2 mg/kg. Considering a crystal content of 30–47 vol.%, and a DRE volume of 0.13 km^3 we find that about 0.05–0.18 Mt SO_2 could have been outgassed from the melt during the eruption (Table 8). These values partly overlap with but is lower than the amount detected from space-borne sensing. This implies that about 0.01–0.12 Mt SO_2 could be stored in an exsolved fluid phase at pre-eruptive conditions. We acknowledge that these values are likely underestimates of the true amount of exsolved fluid phase from the eruption. Uncertainties include maximum melt inclusion SO_2 content being unknown, errors related to the SO_2 detected from satellite, instrumental errors during analyses of glasses on the EPMA, and uncertainties related to erupted volume estimation from deposits used to scale the degassed SO_2 content.

Timescales of magmatic processes

We find that Mg/Fe concentration profiles of reversely zoned Opx crystals in the main- and late-stage pumices yield overlapping timescales (Fig. 12). Timescales of Opx crystals range from about a couple of weeks to up to three months using the Mg-Fe inter-diffusion coefficient from Dohmen *et al.* (2016), which are about a factor of 3 shorter when using the diffusion coefficient from Ganguly & Tazzoli (1994). On the other hand, timescales from Cpx profiles vary from

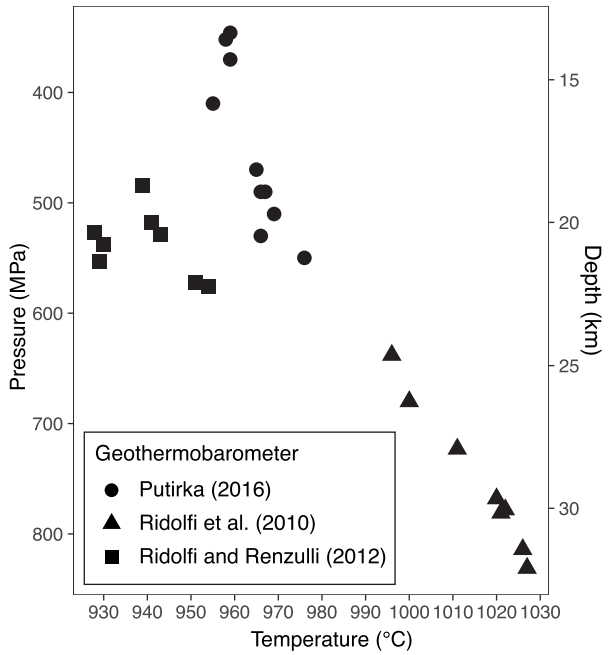

Fig. 10. P–T storage condition of the 1990 magma estimated from amphibole composition in pumices from the main eruptive stage using the different geothermometers. Storage conditions were computed by using the Amph-melt geothermometer of Putirka (2016) (± 30°C; ± 100 MPa), as well as the Amph chemometric formulations by Ridolfi *et al.* (2010) (± 22°C; ± 210 MPa) and Ridolfi & Renzulli (2012) (± 24°C; ± 91 MPa).

one to three months. Bearing this in mind, the Opx timescales better overlap better with those of Cpx when using the diffusion coefficient of Dohmen *et al.* (2016) rather than Ganguly & Tazzoli (1994). Hereafter we refer to the computed timescales from Dohmen *et al.* (2016), which appear more consistent with the recorded length of the pre-eruptive signals.

DISCUSSION

A range of pre-eruptive storage conditions in Kelud's plumbing system

Kelud volcano has consistently erupted basaltic andesite magma for over a hundred years (Bourdier *et al.*, 1997; Humaida, 2013; Jeffery *et al.*, 2013). The main-stage and late-stage pumice samples from the 1990 eruption have both this same composition and display mineralogical and textural features broadly similar to previously erupted products. However, the late-stage pumices are more crystal-rich, have a more evolved glass composition, and record lower temperatures than the main stage pumices, and thus the magma was stored at cooler pre-eruptive conditions.

Our geothermobarometry results indicate that the highest temperatures are about 1050°C and recorded by Opx and Cpx cores in both main-stage and late-stage pumices (Fig. 8), and match the liquidus temperature of the whole-rock with 3 wt.% water in the melt. These temperatures are also consistent with the estimates of Cassidy *et al.* (2019, 2016) for the 2014 eruption using the Plag-melt equilibria and experiments. Pyroxene rim compositions give lower temperatures of around 980°C. Isobaric MELTS modelling at 100 MPa and with 3 wt.% water in the melt indicates that at the above temperature range plagioclase is $An_{84–89}$, which is the composition of the mantle zones of the Plag phenocrysts. Amphibole temperatures calculated following Putirka (2016) are similar to that of pyroxene rims (about 970°C), but much lower temperatures of about 800°C were obtained with the Mag-Ilm equilibria in the late-stage samples. Colder storage conditions for the late-stage magma are also indicated by the presence of quartz and the lower An (= 40) of Plag rims compared to those from the main-stage Plag rims ($An_{58–70}$; Fig. 7a). Oxygen fugacity constrained from the Fe-Ti oxide equilibria in the late-stage pumice indicate relatively oxidizing conditions of about 1 log unit above the NNO buffer.

Mineral-melt equilibria data indicates that the melt could have contained up to 3–4 wt.% dissolved water, which is high enough to stabilize amphibole in a range of typical arc compositions (Costa *et al.*, 2013; Sisson & Grove, 1993). Although amphibole phenocrysts were found in the rocks, amphibole pseudomorphs are more common, and thus magmas were stored close to the stability field of amphibole. Our pre-eruptive pressure estimates from Amph and Plag hygrometry-H_2O/CO_2 saturation suggest that Kelud's plumbing system also has a significant vertical extent. Volatile saturation pressures (110–170 MPa) correspond to 4–9 km depth (using an average local crustal density of 2640 kg m^{-3}; Smyth *et al.*, 2007). A caveat to these depths is that given the minimal value represented CO_2 content used in these calculations from Cassidy *et al.* (2016), these pressures and depth estimates are likely minima values. Recalculation of these saturations and pressures with the scaled fluxed CO_2 content from VolatileCalc and zoned Opx (437 ppm) increases the saturation pressure to 160–190 MPa, which corresponds to 6–8 km depth using the same local crustal density (Table 6). On the other hand, pressure estimates from amphibole phenocrysts correspond to about 15–19 km depth (Fig. 10). Previous studies have suggested that the magma plumbing system of at Kelud may extend to 30 km depth beneath the volcano (Jeffery *et al.*, 2013) so it is possible that part of the crystal cargo from the 1990 eruption could have formed deeper than we have estimated. Thus, our data and those from the literature suggest that the magma plumbing system of Kelud is extended vertically and includes thermally zoned magma storage levels of at least 15 km (see Fig. 11). In addition, mass balance calculations of the sulphur budget (see section 4.3) indicate that the magma coexisted with an exsolved volatile phase at pre-eruptive conditions.

In summary, we propose that before the 1990 eruption, the Kelud plumbing system contained melts and crystals from about 4 km but up to 19 km depth below the crater, with temperatures ranging from 980–1030°C, and water contents in the melt of 2–4 wt.% from which the main-stage magma originated (Fig. 11). The reservoir also contained an exsolved fluid phase before magma ascent towards the surface. The geometry of the plumbing system was such that allowed for the coexistence of magmas with a range of crystallinities and interstitial melt composition. The hotter and less crystal-rich of the central parts erupted as the main phase magma, whereas colder (down to ~800°C), and more crystal-rich parts of the margins produced the late-stage magmas. Hence, it is likely that the magma reservoir beneath Kelud is thermally zoned, with storage temperatures varying from ~750°C (lowest estimate from Mag-Ilm) at its margins to ~980°C in more inner zones (average of pyroxene-melt rim temperatures), and to ~1030°C in its central part (average of pyroxene-melt core temperatures). Such range of temperatures can also explain the abundant presence of a variety of glomerocrysts that could be parts of the higher crystallinity and colder regions of the plumbing system (e.g. Nakada *et al.*, 1994).

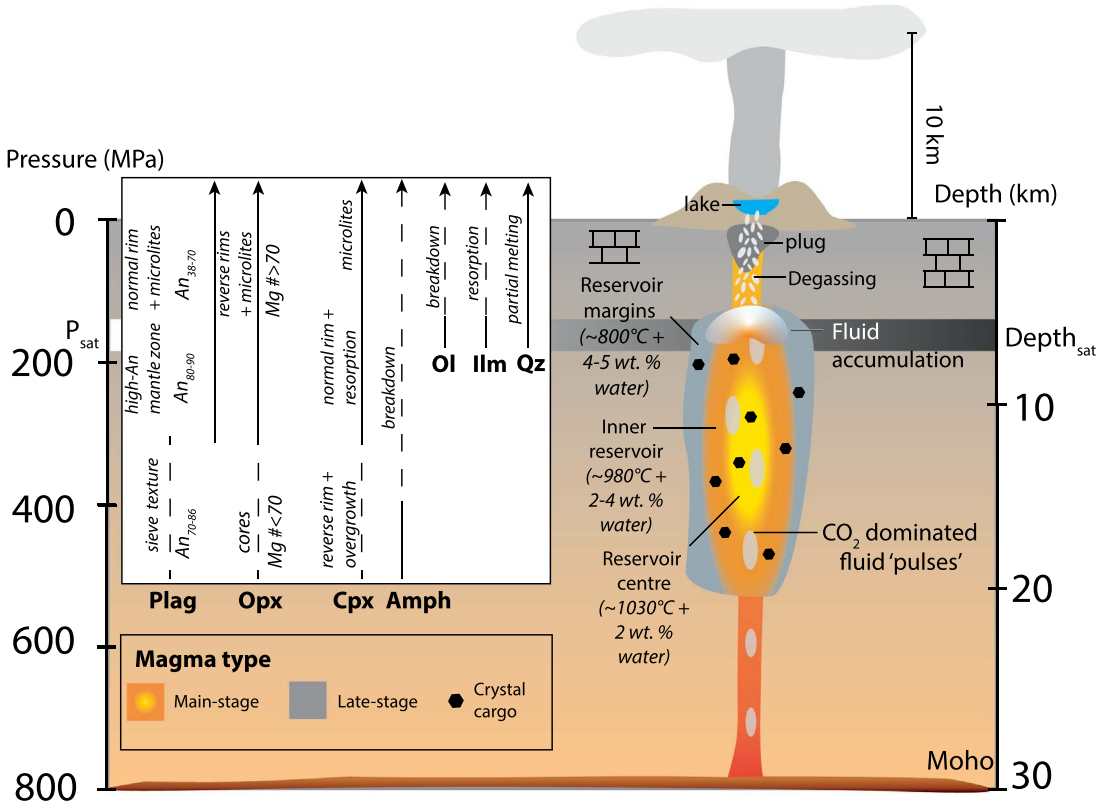

Fig. 11. Schematic cartoon of Kelud's plumbing system according to petrologic observations and geothermobarometric estimates and of the pre-eruptive processes that most likely drove the 1990 eruption. The magma reservoir is likely to be zoned both in temperature (°C) and water content (wt.%). Inset white box summarizes the corresponding mineral textures and compositions. Distinct magma types from the main and late stages along with their crystal cargoes are shown in the drawing. The fluxing of CO_2 dominated fluid from depth as well as the creation of an exsolved fluid phase in the shallow parts of the system are also highlighted and considered key for driving the short-lived explosive eruptions of Kelud. The brick-like pattern represents the volcaniclastic crustal sediments and carbonates that are found underneath Kelud (Jeffery *et al.*, 2013 and references therein).

Magmatic processes and timescales related to the 1990 eruption

Relating mineral textures and chemistry to pre-eruptive processes

Many studies have proposed that intrusion of primitive magma and mixing are the main processes commonly driving volcanic eruptions, as the influx of more mafic hotter and volatile-rich magma can build enough overpressure (Costa & Chakraborty, 2004; Folch & Martí, 1998; Huppert *et al.*, 1982). Moreover, mafic magma intrusion has also been proposed based on textural evidence of the crystal cargo, including multimodal core and rim mineral compositions, reverse zoning of Mg-number in mafic minerals such as pyroxenes, and of An in plagioclase (Streck, 2008). We found that Opx and Cpx show limited range in compositional zoning in Mg-number or are reversely zoned, with rims that have higher Mg-number than the cores. This is especially true for Opx in the main-stage magma (23% of the Opx population surveyed). Although the reverse zoning in Opx could be interpreted as evidence of input of more primitive melt before the eruption, we would also expect to find reverse zoning in plagioclase, but this is not the case. We also did not find the typical bimodal crystal populations that appears in many systems where intrusion of primitive magma has been recognized. Moreover, the calculated temperature of the Opx rims and the cores overlaps, or the rims yield somewhat lower temperatures despite having high Mg-number. An alternative possibility in relating these observations with their magmatic processes is that the reverse zoning in Opx reflects an increase in oxygen fugacity and/or a decrease of the water content in the melt. Waters & Lange (2017) found a systematic increase of the Mg-number of the Opx as the water content in the melt decreases, and they experimentally calibrated a relationship between the two variables. We have exploited this finding by applying the experimental ${}^{Fe^{2+}-Mg}K_d$ relationship to find the change in water composition corresponding to the change observed between rim and core compositions i.e.:

$$\Delta^{Fe^{2+}-Mg}K_d = \left(\left[\left(X_{MgO}^{liquid}X_{FeO}^{opx}\right]/\left[X_{FeO}^{liquid}\ X_{MgO}^{opx}\right]\right)_{core} - \left(\left[\left(X_{MgO}^{liquid}X_{FeO}^{opx}\right]/\left[X_{FeO}^{liquid}\ X_{MgO}^{opx}\right]\right)_{rim} \quad (2)$$

From this, it is apparent that a decrease of water in the melt of up to ~2 wt.% from the Opx core to the rim (Fig. 9b) can explain the increase of Mg-number of the Opx cores (67–70) to the rims (70–72). Such a water decrease would also lead to crystallization and normal zoning in plagioclase, and thus would explain several of the textural and compositional features of Opx and Plag. The observed water decrease in the melt could be related to magma degassing and ascent towards the surface, and/or fluxing of the reservoir by CO_2 dominated fluids from depth as we discuss below.

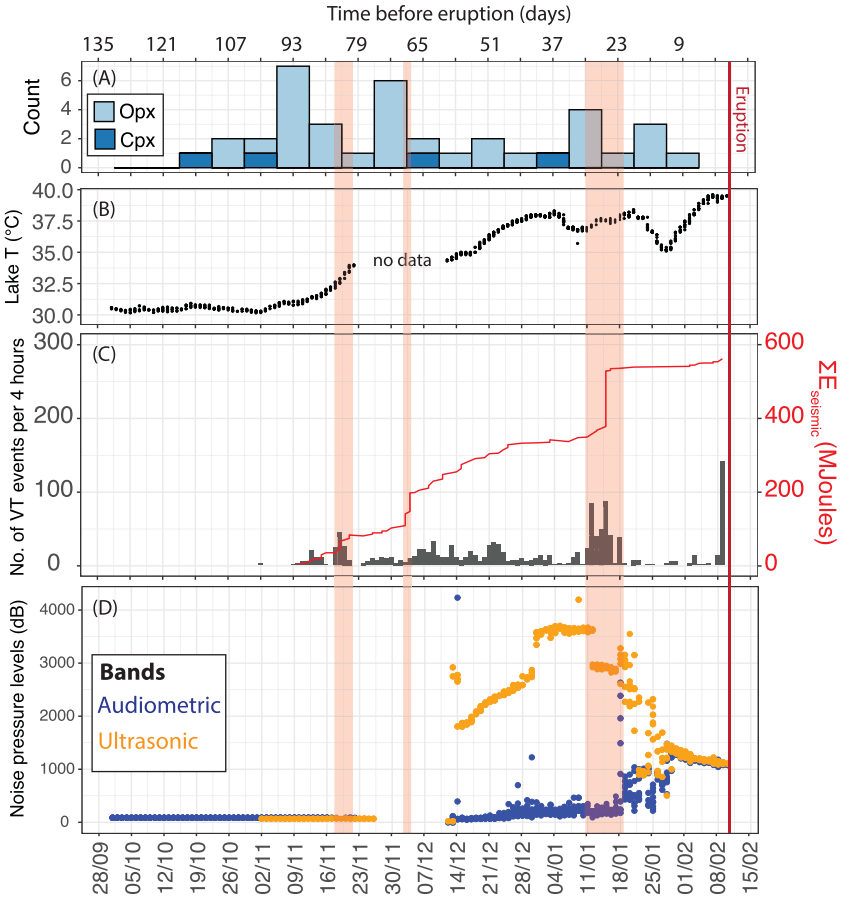

Fig. 12. (a) Histogram of calculated Opx and Cpx diffusion timescales (recalculated dates before the 1990 eruption day) compared to the pre-eruptive temporal evolution of (b) crater lake temperature (Vandemeulebrouck *et al.*, 2000); (c) seismicity (black histogram = number of VT events per hours, red line = cumulative seismic energy) (Lesage and Surono, 1995); and (d) hydroacoustics (audiometric and ultrasonic bands) signals (Vandemeulebrouck *et al.*, 2000). Vertical bands highlight the timing of seismic swarms and ae used a visual guidance and comparison to changes in other data. The missing data interval in lake temperature and hydroacoustics was due to power supply failure.

Fluid fluxing from depth and creation of an exsolved volatile phase

In recent years it has become apparent that in addition to replenishment by a more primitive melt, magma plumbing systems may be fluxed by hot volatiles arising from the deeper part of the magma system (Mastin and Witter, 2000; Spilliaert *et al.*, 2006; Giuffrida *et al.*, 2017; Flaherty *et al.*, 2018; Hartung *et al.*, 2019). Petrological analysis of melt inclusions and modeling support this possibility, and such fluid addition from depth can also account for the permanent volcanic plumes of many mafic volcanoes. Given the dependency of different volatile elements with pressure, the deeper parts of the system are typically CO_2-rich, because CO_2 is much less soluble than water and SO_2, and can thus degas earlier and flux through the upper parts of the system, with mechanisms that may include channeling (Caricchi *et al.*, 2018; Collombet *et al.*, 2021; Giuffrida *et al.*, 2017; Spilliaert *et al.*, 2006). CO_2 fluxing can have widespread effects on a shallow magmatic system that vary depending on the pressure, but include the crystallization of high-Mg, high-Ca pyroxene rims (Giuffrida *et al.*, 2017). Thus, we propose that addition of CO_2-rich fluids from depth may have decreased the water fugacity and thus water content of the melt in the shallower parts of the Kelud magmatic system and may explain the reverse zoning of Opx, normally zoned Plag, and the Cpx overgrowths and reverse zoning of some Cpx in our samples (Fig. 4d).

Mass balance constraints on fluid fluxing

Quantifying the CO_2 that may have fluxed through the system is challenging because it is a dynamic process. There are no measurements of pre-eruptive/syn-eruptive CO_2/SO_2 and H_2O/CO_2 values of the gases for the 1990 eruption, although some fumaroles were measured in 1978 ($H_2O/CO_2 = 17$) and after the eruption in August 1990 ($H_2O/CO_2 = 7.7$) (Global Volcanism Program, 1990). Moreover, although melt inclusion compositions can be in principle used to identify the CO_2 fluxing (Wallace, 2005) it is becoming increasingly apparent that a significant part of the CO_2 can be trapped in bubbles inside the inclusion, and thus the data is also difficult to interpret in terms of fluid fluxing. To test the CO2 fluxing hypothesis we propose, we have performed a series of calculations based on some observations and mass balance as we describe below.

The change in Mg-Fe in reversely zoned Opx can be explained by a water loss of the melt from about 4 wt.% to about 2 wt.% (section 5.2.1, Fig. S6), which we propose it is due to addition of CO_2 of mafic magma from depth or limestone assimilation. Assuming that the melt is fluid saturated, we calculated the concentration of CO_2 that would need to be added to the melt to decrease the water content in the melt from about 4 to 2 wt.% (Table 6). For this we used two end-member cases of the initial (pre- fluxing) CO_2 concentration in the melt, one close to zero and another of 336 ppm as measured

Table 6: mass balance calculations for CO_2 dominated fluid flushing and comparison of accumulation times using flux rates Javanese volcanoes

1. Melt volatile content	
1a. Initial melt volatile content	Volatile content
H_2O (wt.%)	3.8–5
CO_2 (ppm)	336–0
1b. Final melt volatile content	
H_2O (wt.%)	2.0
CO_2 (ppm)	759
1c. Change in melt volatile content	
H_2O (wt.%)	1.8–3.0
CO_2 (ppm)	423–759
2. Mass balance of amount of CO_2 fluxed	
Erupted volume (DRE) (km^3)	0.13
Rock density (kg m^{-3})	2402
Mass of magma (Mt)	312
Melt proportion	0.58
Mass of melt (Mt)	180
	Range
Fluxed CO_2 (ppm)	244–437
Fluxed CO_2 (Mt)	0.08–0.14
3. Amount of limestone vs. mafic magma degassing needed for CO_2 flushing	
3a. Effect of limestone assimilation	
CO_2 in pure limestone (wt.%)	44
Mass of limestone (Mt)	0.13–0.23
Volume of limestone[&] (m^3)	84 840
3b. Effect of degassing basaltic magma[#]	
CO_2 content in wt.%	Mass of basaltic melt (Mt)
0.5	15–31
1	27–55
	Volume of basaltic melt[*] (m^3)
0.5	5034–10 403
1	9060–18 456
4. Time needed to produce total 0.08–0.14 CO_2 using degassing data of Javanese volcanoes[‡]	
Volcano	CO_2 degassing (tonnes/day)
Merapi	104
Bromo-Semeru	2184
Raung-Ijen	1111
	Time (days)
Merapi	1346
Bromo-Semeru	64
Raung-Ijen	126

[$]Maximum CO_2 content taken from Cassidy *et al.* (2016)

[#]Range of CO_2 content taken from arc basalts (min CO_2 from modal CO_2 content from Galunggung [Sisson and Bronto, 1988]; max CO_2 content from Cerro Negro [Lowenstern, 2001])

[‡]CO_2 fluxes from Javanese volcanoes Aiuppa *et al.* (2019)

[&]Density of pure calcite = 2711 kg m-3 (https://www.mindat.org/min-859.html)

[*]Density of wet basalt = 2980 kg m-3 (Sharma, 1997, p. 17)

in melt inclusions from the 2014 magma (Cassidy *et al.*, 2016). We found that for these two end members, the melt would have gained about 420 ppm to 760 ppm CO_2. Taking into account the crystal proportions and volume of the eruption (DRE) (which corresponds to 180 Mt of erupted magma) gives that between about 0.08 to 0.14 Mt of CO_2 should have been added to the melt.

To further test whether these are realistic amounts of CO_2 we also calculated: (1) the mass of pure limestone and basaltic magma that would be need to degas to generate such masa of CO2, and (2) the time that would be required to degas such amount of CO2 using the degassing fluxes from other open vent volcanoes in Java. We describe these below in two sections., and where our calculations are summarized in Table 6. Such sources of CO_2-dominated fluids could come from the degassing of deep-seated basaltic magma, for example at Cerro Negro (Lowenstern, 2001) or Galunggung (Sisson & Bronto, 1998), or from assimilation of limestone or volcaniclastic crustal sediment underlying Kelud that commonly underlie active volcanoes along the Sunda Arc. Calc-silicate skarn xenoliths have been found in rocks from the more recent 2007 dome (Jeffery *et al.*, 2013), and crustal limestones also outcrops in some localities around East Java (e.g. Smyth *et al.*, 2007). Jeffery *et al.* (2013) suggested that crustal assimilation likely came from volcaniclastic crustal sediment making up most of the country rock (~25% contamination), with limestone and skarns possibly making up smaller portions, as well. This contrasts with other volcanoes such as Merapi, where limestone is the dominant source of crustal contaminant (Handley *et al.*, 2014). The process of crustal CO_2 assimilation reaction at volcanoes such as Merapi (Central Java, Indonesia) is shown to enhance the intensity of explosive eruptions by a factor of 3–5 (Troll *et al.*, 2012), and could make a significant contribution to the overall volatile budget of the magma (Deegan *et al.*, 2010). Thus, we calculated the amount of mass contribution of either limestone assimilation or basalt degassing from depth to produce the change in CO_2 in the melt that we have estimated (Table 6). Here we assume that the entirety of the CO_2 exsolved originates either from limestone assimilation or degassing of basaltic magma. We used the stoichiometric concentration of CO_2 in pure limestone, and basaltic magma containing 0.5–1 wt.% CO_2. We find that it would require up to 0.13–0.23 Mt of limestone or CO_2 from 15–55 Mt basaltic magma, although this is likely an underestimation. These masses are much smaller than the total amount of magma erupted, and thus they seem realistic.

Finally, it is also worth evaluating whether accumulating such an amount of CO_2 fluid before eruption is realistic. To do this, we consider CO_2 fluxes from passively degassing volcanic plumes of volcanoes that are similar to Kelud in terms of magma composition, tectonic setting, and geographical location, as we do not have CO_2 fluxes from Kelud itself. Aiuppa *et al.* (2019) reported 104 tonnes/day of CO_2 for Merapi, 1.1 kt/day for Raung-Ijen, and 2.1 kt/day for Bromo-Semeru. Using a range of these values (Table 6) we find that to flux 0.14 Mt would require CO_2 fluxes between that of Bromo-Semeru (2.2 kt/day or 64 days) and Raung-Ijen (1.1 kt/day or 126 days). These times are short compared to the inter-eruptive repose at Kelud of several years, and thus our estimates of accumulation time also seem realistic. In summary, we believe that it is possible that the estimated amount of fluids can flux through Kelud's magmatic system and accumulate months before eruption.

Regardless of its source, volatile fluxing can thus affect the textures and compositions of minerals without necessarily affecting the bulk rock composition, if no crystal cargo were brought up with the volatiles. Most importantly, CO_2 fluxing favors the exsolution of water and thus a dehydration of the melt (Spilliaert *et al.*, 2006), thereby promoting enhanced magma crystallization as well as the

Table 7: Petrologic calculations of outgassed SO_2 with satellite (TOMS) detection of SO_2 emissions, following the methodology of Jay *et al.* (2014)

1. Kelud's excess SO_2 gas	KELUD1990-PL1	90–23	Units
Erupted volume (DRE)	0.13	0.13	km^3
Rock density	2352	2402	kg/m^3
Mass of magma	306	312	Mt
Concentration of SO_2 melt Inclusion	1110	440	ppm
Concentration of SO_2 interstitial glass	60	90	ppm
Glass proportion	0.69	0.53	
2. Petrologic calculations			
SO_2 degassed from the melt	0.18	0.05	Mt
3. Volcanic gas satellite measurements			
Atmospheric SO_2	0.17	0.17	Mt
Excess SO_2 exsolved from melt	0.01	0.12	Mt

accumulation of an exsolved fluid phase. Fluid addition dominated by CO_2 from depth or through crustal contamination plus crystallization at the shallow parts of the plumbing system can lead to melt supersaturation in volatiles, and the creation of an exsolved volatile phase, for which we have found also evidence using the SO_2 budget of the eruption (Table 7). Given that Kelud is a semi-plugged stratocone (Whelley *et al.*, 2015), fluid accumulation in the reservoir is possible and may lead to the overpressure necessary to promote explosive eruption (Stock *et al.*, 2016). Various studies of the 2014 eruption have also proposed that this eruption of Kelud was probably driven by volatile accumulation rather than magma replenishment, in a similar manner to that of the 2014 eruption and the Calbuco 2015 eruption in Chile (Arzilli *et al.*, 2019; Cassidy *et al.*, 2019; Namur *et al.*, 2020; Pardini *et al.*, 2018).

Time scales of processes and relation to monitoring data

The monitoring records that we have compiled may also be related to fluid movement and accumulation prior to the 1990 eruption and which were captured as unrest signals. Vandemeulebrouck *et al.* (2000) showed that the baseline low frequency hydroacoustic noise started to increase as far back as April 1989. Although the baseline increase was lower than the unrest observed between November and February, this could indicate that the volatile pressure had increased enough to allow gases to leak to the surface and reach the bottom of the lake. In the November–February unrest period there is a stepwise increase in lake temperature, with a temporary dip in January due to a short rainfall episode (Fig 12b). This trend in lake temperature is accompanied by a significant increase in the hydroacoustic noise level in the ultrasonic band after the November swarm (Fig 12d). However, ultrasonic noise levels declined after the January swarm until just before the eruption, in contrast with the gradual increase in audiometric noise level. Vandemeulebrouck *et al.* (2000) interpreted these variations as the hydrothermal system opening up to prime for an eruption, with the drop in January reflecting a large outgassing episode into the lake.

In addition to the hydroacoustic record, the unrest include two major VT seismic swarms in November and January, accompanied by sharp pulses in seismic energy release (Fig 12c) (Lesage & Surono, 1995). Between these swarms, there is incremental increase in both number of VT earthquakes and a minor spike in seismic energy release. Lesage & Surono (1995) interpreted these patterns in seismicity as originating from the brittle plug fracturing and opening of the system. Thus, it seems possible that the plug was fractured from a combination of pulses of fluid fluxing (seismic swarms) and accumulation of fluids exerting overpressure on the plug (incremental increase in seismicity). Our interpretation of the changes in Mg-number of pyroxene (reversely zoned crystals) is that they record a decrease in the water content in the melt due to CO_2-dominated fluids from depth (basaltic magma or limestone degassing) rather than more primitive magma intrusion. Our models of equilibration of the Fe/Mg zoning of these same pyroxenes gave times of 2–3 months before the eruption, which is within the duration of unrest signals in both the seismicity (Lesage & Surono, 1995), crater lake temperature, and hydroacoustics (Vandemeulebrouck *et al.*, 2000) (Fig. 12a-d). However, we do not observe an exact match between timing of the crystals and the changes of the monitoring parameters. Crystal zoning timescales precede the recorded seismic swarms or spikes in seismic energy by up to a week, and steep increases of the lake temperature and/or hydroacoustic signals by up to two weeks. This is different from other studies where the match between the crystal zoning and seismicity has been reported (Costa *et al.*, 2020; Kahl *et al.*, 2011; Saunders *et al.*, 2012). Although we do not have enough data in crystal zoning to make it a statistically robust observation, such a time difference could be related to the lag of time between the phenomena of fluid percolation from depth and the processes that are responsible for the changes in seismic data and water lake changes. Finally, we emphasize that our diffusion timescales are considerably longer than what would be expected for a simple process of magma decompression and ascent from depth and thus the zoning recorded in the pyroxenes is more likely due to the fluid fluxing than simple magma ascent. As noted in the previous section, it seems possible to add the necessary mass of CO_2 to the system in times of a few months and thus it is compatible with duration of the unrest and also with the time scales of the crystals.

A general model for Kelud eruptions and their relation to other volcanoes

We believe that a simple conceptual model to explain the explosive (e.g. VEI 4) but short-lived eruptions, that have limited unrest until

very close to the eruption is the accumulation of a pre-existing volatile phase over time, and especially the addition of fluids from depths that may overpressure the system to fracture the plug. The resulting eruption is highly explosive but very brief, because it is mainly driven by accumulated fluids in the upper parts of the system. The monitoring data show that for volcanoes with a water lake, it might be possible to identify when the fluid pressure has become large enough for gases to start leaking towards the surface and affect the hydroacoustics and lake temperature. Although changes in seismicity occur much closer to eruption, especially the exponential increases that are typically associated with run-away processes and failure of the rocks (e.g. Nakamichi *et al.*, 2017).

Fluid accumulation may also explain why these eruptions also show limited unrest in terms of signals and duration, whereas we would expect renewed intrusions with more primitive magma and the significant addition of mass to have much stronger signals, especially seismicity as seen at other volcanoes such as Soufrière Hills, Montserrat (Murphy *et al.*, 1998; Plail *et al.*, 2018), Tungurahua (Myers *et al.*, 2014; Samaniego *et al.*, 2011), and Ruapehu (Conway *et al.*, 2018; Kilgour *et al.*, 2013). From a petrologic and monitoring perspective, we can consider the 2014 eruption of Kelud as an intra-volcanic analogue to the 1990, as it was quite similar in many volcanological and petrological attributes to the 1990 eruption. In turn, the 1990 and 2014 eruptions are similar to the VEI 4 explosive eruption of Calbuco volcano in 2015. Prior to the 2015 eruption, Calbuco also had a protracted repose time with the last recorded activity in 1996, yet experienced a short and subdued unrest of only 2–3 hours before erupting explosively (VEI 4) (Global Volcanism Program, 2015). The similarities between these different eruptions and volcanoes may indicate that they operate by similar processes, and that fluid fluxing from depth accompanied by accumulation of a pre-existing volatile phase can be a major scenario to be considered for future events (e.g. Petrelli *et al.*, 2018).

CONCLUSION

The combined petrological and monitoring data we report for the Kelud 1990 eruption suggest that the explosive but short-lived event was probably driven by accumulation of exsolved fluids at the top of the plumbing system. Fluxing of CO_2-dominated fluids from depth was likely a main contributor to the over pressures that eventually broke a plugged conduit necessary for the eruption to occur. The fluid fluxing promoted partial dehydration of the magma, leading to crystallization and second boiling and additional fluid exsolution. Diffusion profiles in zoned pyroxene crystals allow us to infer fluid fluxing and overpressure build up in the shallow magmatic system began 2–3 months before the eruption. This time frame which matches with the onset and duration of both seismic and crater lake unrest signals. The conceptual model we propose is likely applicable to other short-lived but explosive eruptions with limited unrest such the 2014 Kelud eruption or the 2015 Calbuco in Chile.

SUPPLEMENTARY DATA

Supplementary data are available at *Journal of Petrology* online.

ACKNOWLEDGEMENTS

We thank C.Widiwijayanti, S.Jenkins, J.Herrin, J. Oalmann, L. Cheng, G. Fabbro, R.I. Made, D. Schonwalder, L. Siang Joo, and E. Y. Yin for assistance with sample preparation, analyses and discussions on the Kelud volcano system. We also thank student assistants W. Wijaya and J. Fu for digitizing historical unrest records. Thanks also go to J. Vandemeulebrouck for providing the original dataset for the hydroacoustic measurements. We thank Fabio Arzilli, Frances Deegan, and an anonymous reviewer for their insightful comments that improved our manuscript considerably. This research was supported by the Earth Observatory of Singapore via its funding from the National Research Foundation Singapore and the Singapore Ministry of Education under the Research Centres of Excellence initiative. F. Costa was funded by NRFi Award (NRF-NRFI2017-06). The data underlying this article are available in the article and in its online supplementary material.

REFERENCES

Aiuppa, A., Fischer, T. P., Plank, T. & Bani, P. (2019). CO 2 flux emissions from the Earth's most actively degassing volcanoes, 2005–2015. *Science Reports* **9**, 2005–2015. https://doi.org/10.1038/s41598-019-41901-y.

Albert, H., Costa, F., Di Muro, A., Herrin, J., Métrich, N. & Deloule, E. (2019). Magma interactions, crystal mush formation, timescales, and unrest during caldera collapse and lateral eruption at ocean island basaltic volcanoes (piton de la Fournaise, La Réunion). *Earth and Planetary Science Letters* **515**, 187–199. https://doi.org/10.1016/j.epsl.2019.02.035.

Albert, H., Costa, F. & Martí, J. (2016). Years to weeks of seismic unrest and magmatic intrusions precede monogenetic eruptions. *Geology* **44**, 211–214. https://doi.org/10.1130/G37239.1.

Andersen, D. J., Lindsley, D. H. & Davidson, P. M. (1993). QUILF: a pascal program to assess equilibria among FeMgMnTi oxides, pyroxenes, olivine, and quartz. *Computers and Geosciences* **19**, 1333–1350. https://doi.org/10.1016/0098-3004(93)90033-2.

Andreastuti, S., Paripurno, E. T., Gunawan, H., Budianto, A., Syahbana, D. & Pallister, J. (2019). Character of community response to volcanic crises at Sinabung and Kelud volcanoes. *Journal of Volcanological and Geothermal Research* **382**, 298–310. https://doi.org/10.1016/j.jvolgeores.2017.01.022.

Arzilli, F., Morgavi, D., Petrelli, M., Polacci, M., Burton, M., Di Genova, D., Spina, L., La Spina, G., Hartley, M. E., Romero, J. E., Fellowes, J., Diaz-Alvarado, J. & Perugini, D. (2019). The unexpected explosive sub-Plinian eruption of Calbuco volcano (22–23 April 2015; southern Chile): Triggering mechanism implications. *Journal of Volcanological and Geothermal Research* **378**, 35–50. https://doi.org/10.1016/j.jvolgeores.2019.&break;04.006.

Badrudin, M. (1994). Kelut volcano monitoring: Hazards, mitigation and changes in water chemistry prior to the 1990 eruption. *Geochemical Journal* **28**, 233–241.

Bernard, A. & Mazot, A. (2004). Geochemical evolution of the young crater lake of Kelud volcano in Indonesia. In: Wanty, R.B. (ed.). In: *Water-Rock Interaction (WRI-11). Rotterdam: A.A. Balkema*, pp. 87–90.

Blake, D. M., Wilson, G., Stewart, C., Craig, H., Hayes, J. L., Jenkins, S. F., Wilson, T. M., Horwell, C. J., Daniswara, R., Ferdiwijaya, D. & Leonard, G. S. (2015). Impacts of the 2014 eruption of Kelud volcano, Indonesia, on infrastructure, utilities, agriculture and health. *GNS Science Report, 15*.

Bourdier, J. L., Pratomo, I., Thouret, J. C., Boudon, G. & Vincent, P. M. (1997). Observations, stratigraphy and eruptive processes of the 1990 eruption of Kelut volcano. *Clinical and Laboratory Standards Institute (Series)* **79**, 181–203.

Bucholz, C. E., Gaetani, G. A., Behn, M. D. & Shimizu, N. (2013). Post-entrapment modification of volatiles and oxygen fugacity in olivine-hosted melt inclusions. *Earth and Planetary Science Letters* **374**, 145–155. https://doi.org/10.1016/j.epsl.2013.05.033.

Caricchi, L., Biggs, J., Annen, C. & Ebmeier, S. (2014). The influence of cooling, crystallisation and re-melting on the interpretation of geodetic signals in volcanic systems. *Earth and Planetary Science Letters* **388**, 166–174. https://doi.org/10.1016/j.epsl.2013.12.002.

Caricchi, L., Sheldrake, T. E. & Blundy, J. (2018). Modulation of magmatic processes by CO2 flushing. *Earth and Planetary Science Letters* **491**, 160–171. https://doi.org/10.1016/j.epsl.2018.03.042.

Carn, S. (2019). *Multi-Satellite Volcanic Sulfur Dioxide L4 Long-Term Global Database* , V3. https://doi.org/10.5067/MEASURES/SO2/DATA404.

Carn, S. A., Yang, K., Prata, A. J. & Krotkov, N. A. (2015). Extending the long-term record of volcanic SO2 emissions with the ozone mapping and profiler suite nadir mapper. *Geophysical Research Letter* **42**, 925–932. https://doi.org/10.1002/2014GL062437.

Cassidy, M., Castro, J. M., Helo, C., Troll, V. R., Deegan, F. M., Muir, D., Neave, D. A. & Mueller, S. P. (2016). Volatile dilution during magma injections and implications for volcano explosivity. *Geology* **44**, 1027–1030.

Cassidy, M., Ebmeier, S. K., Helo, C., Watt, S. F. L., Caudron, C., Odell, A., Spaans, K., Kristianto, P., Triastuty, H., Gunawan, H. & Castro, J. M. (2019). Explosive eruptions with little warning: experimental petrology and volcano monitoring observations from the 2014 eruption of Kelud, Indonesia. *Geochemistry, Geophysics, Geosystems* **20**, 4218–4247. https://doi.org/10.1029/2018gc008161.

Caudron, C., Mazot, A. & Bernard, A. (2012). Carbon dioxide dynamics in Kelud volcanic lake. *Journal of Geophysical Research: Solid Earth* **117**, B05102.

Cheng, L. & Costa, F. (2019). Statistical analysis of crystal populations and links to volcano deformation for more robust estimates of magma replenishment volumes. *Geology* **47**, 1171–1175. https://doi.org/10.1130/G46826.1.

Chiarabba, C., De Gori, P. & Patanè, D. (2004). The Mt. *Mt. Etna: Volcano Laboratory* **143**, 191–204. https://doi.org/10.1029/143GM12.

Collombet, M., Burgisser, A., Colombier, M. & Gaunt, E. (2021). Evidence for deep gas loss in open volcanic systems. *Bulletin of Volcanology* **83**. https://doi.org/10.1007/s00445-020-01433-0.

Conway, C. E., Gamble, J. A., Wilson, C. J. N., Leonard, G. S., Townsend, D. B. & Calvert, A. T. (2018). New petrological, geochemical, and geochronological perspectives on andesite-dacite magma genesis at Ruapehu volcano, New Zealand. *American Mineralogist* **103**, 565–581. https://doi.org/10.2138/am-2018-6199.

Costa, F., Andreastuti, S., Bouvet de Maisonneuve, C. & Pallister, J. S. (2013). Petrological insights into the storage conditions, and magmatic processes that yielded the centennial 2010 Merapi explosive eruption. *Journal of Volcanological and Geothermal Research* **261**, 209–235. https://doi.org/10.1016/j.jvolgeores.2012.12.025.

Costa, F. & Chakraborty, S. (2004). Decadal time gaps between mafic intrusion and silicic eruption obtained from chemical zoning patterns in olivine. *Earth and Planetary Science Letters* **227**, 517–530.

Costa, F., Dohmen, R. & Chakraborty, S. (2008). Time scales of magmatic processes from modeling the zoning patterns of crystals. *Reviews in Mineralogy and Geochemistry* **69**, 545–594.

Costa, F. & Morgan, D. (2010). Time constraints from chemical equilibration in magmatic crystals. In: Dosseto, A., Turner S. P. & van Orman, J. A. (eds) *Timescales of magmatic processes: from core to atmosphere*. West Sussex, UK: Chichester, pp. 125–159.

Costa, F., Scaillet, B. & Gourgaud, A. (2003). Massive atmospheric sulfur loading of the AD 1600 Huaynaputina eruption and implications for petrologic sulfur estimates. *Geophysical Research Letter* **30**, 1–4. https://doi.org/10.1029/2002GL016402.

Costa, F., Shea, T. & Ubide, T. (2020). Diffusion chronometry and the timescales of magmatic processes. *Nature Reviews Earth & Environment* **1**, 201–214. https://doi.org/10.1038/s43017-020-0038-x.

Deegan, F. M., Troll, V. R., Freda, C., Misiti, V., Chadwick, J. P., McLeod, C. L. & Davidson, J. P. (2010). Magma–carbonate interaction processes and associated CO2 release at Merapi volcano, Indonesia: Insights from experimental petrology. *Journal of Petrology* **51**, 1027–1051. https://doi.org/10.1093/petrology/egq010.

Deer, W. A., Howie, R. A., Zussman, J. (1992).. An introduction to the rock-forming minerals, 2nd ed. Harlow: Longman Scientific & Technical.

Devine, D., Siggurdson, H. & Davis, A. N. (1984). Estimates of sulfur and chlorine yield to the atmosphere from volcanic eruptions and potential climatic effects. *Journal of Geophysical Research* **89**, 6309–6325.

Esposito, R., Hunter, J., Schiffbauer, J. D., Shimizu, N. & Bodnar, R. J. (2014). An assessment of the reliability of melt inclusions as recorders of the pre-eruptive volatile content of magmas. *American Mineralogist* **99**, 976–998. https://doi.org/10.2138/am.2014.4574.

Flaherty, T., Druitt, T. H., Tuffen, H., Higgins, M. D., Costa, F. & Cadoux, A. (2018). Multiple timescale constraints for high-flux magma chamber assembly prior to the late bronze age eruption of Santorini (Greece). *Contributions to Mineralogy and Petrology* **173**, 1–21. https://doi.org/10.1007/s00410-018-1490-1.

Folch, A. & Marti, J. (1998). The generation of overpressure in felsic magma chambers by replenishment. *Earth and Planetary Science Letters* **163**, 301–314. https://doi.org/https://doi.org/10.1016/S0012-821X(98)00196-4.

Gaetani, G. A., O'Leary, J. A., Shimizu, N., Bucholz, C. E. & Newville, M. (2012). Rapid reequilibration of H 2O and oxygen fugacity in olivine-hosted melt inclusions. *Geology* **40**, 915–918. https://doi.org/10.1130/G32992.1.

Gaetani, G. A. & Watson, E. B. (2000). Open system behavior of olivine-hosted melt inclusions. *Earth and Planetary Science Letters* **183**, 27–41.

Ghiorso, M. S. & Evans, B. W. (2008). Thermodynamics of rhombohedral oxide solid solutions and a revision of the Fe-Ti two-oxide geothermometer and oxygen-barometer. *American Journal of Science* **308**, 957–1039. https://doi.org/10.2475/09.2008.01.

Ghiorso, M. S. & Gualda, G. A. R. (2015). An H2O–CO2 mixed fluid saturation model compatible with rhyolite-MELTS. *Contributions to Mineralogy and Petrology* **169**, 53.

Giuffrida, M., Holtz, F., Vetere, F. & Viccaro, M. (2017). Effects of CO2flushing on crystal textures and compositions: Experimental evidence from recent K-trachybasalts erupted at Mt. Etna. *Contributions to Mineralogy and Petrology* **172**, 1–18. https://doi.org/10.1007/s00410-017-1408-3.

Global Volcanism Program (2015). Report on Calbuco (Chile). In: Venzke, E. (ed.) *Bulletin of the Global Volcanism Network, 40*. Smithsonian Institution, p. 6. https://doi.org/10.5479/si.GVP.BGVN201506-358020.

Global Volcanism Program. (2013). Kelut (263280) in Volcanoes of the World, v. 4.10.3 (15 Oct 2021). In: Venzke, E. (ed.) Smithsonian Institution. Downloaded 08 Nov 2021 (https://volcano.si.edu/volcano.cfm?vn=263280). https://doi.org/10.5479/si.GVP.VOTW4-2013.

Global Volcanism Program (1990). Report on Kelut (Indonesia). In: McClelland, L. (ed.) *Bulletin of the Global Volcanism Network, 15*. Smithsonian Institution, p. 9. https://doi.org/10.5479/si.GVP.BGVN199009-263280.

Goode, L. (2018). *Investigating the magmatic drivers behind temporal variations in eruption frequency and style at Kelut volcano*. Indonesia.

Goode, L. R., Handley, H. K., Cronin, S. J. & Abdurrachman, M. (2019). Insights into eruption dynamics from the 2014 pyroclastic deposits of Kelut volcano, Java, Indonesia, and implications for future hazards. *Journal of Volcanological and Geothermal Research*. https://doi.org/10.1016/J.JVOLGEORES.2018.02.005.

Gualda, G. A. R., Ghiorso, M. S., Lemons, R. V. & Carley, T. L. (2012). Rhyolite-MELTS: a modified calibration of MELTS optimized for silica-rich, fluid-bearing magmatic systems. *Journal of Petrology* **53**, 875–890.

Handley, H. K., Blichert-Toft, J., Gertisser, R., Macpherson, C. G., Turner, S. P., Zaennudin, A. & Abdurrachman, M. (2014). Insights from Pb and O isotopes into along-arc variations in subduction inputs and crustal assimilation for volcanic rocks in Java, Sunda arc. *Geochimica Cosmochimica Acta* **139**, 205–226.

Hartung, E., Weber, G. & Caricchi, L. (2019). The role of H 2 O on the extraction of melt from crystallising magmas. *Earth and Planetary Science Letters* **508**, 85–96. https://doi.org/10.1016/j.epsl.2018.12.010.

Hidayati, S., Triastuty, H., Mulyana, I., Adi, S., Ishihara, K., Basuki, A., Kuswandarto, H., Priyanto, B. & Solikhin, A. (2019). Differences in the seismicity preceding the 2007 and 2014 eruptions of Kelud volcano, Indonesia. *Journal of Volcanology and Geothermal Research* **382**, 50–67. https://doi.org/10.1016/j.jvolgeores.2018.10.017.

Humaida, H. (2013). A Geochemical Study on Merapi and Kelud Volcanic Eruptions. PhD Thesis, Universitas Gadjah Mada, Yogyakarta, Indonesia (Unpublished).

Huppert, H. E., Sparks, R. S. J. & Turner, J. S. (1982). Effects of volatiles on mixing in calc-alkaline magma systems. *Nature* **297**, 554–557. https://doi.org/10.1038/297554a0.

Jay, J., Costa, F., Pritchard, M., Lara, L., Singer, B. & Herrin, J. (2014). Locating magma reservoirs using InSAR and petrology before and during the 2011–2012 Cordón Caulle silicic eruption. *Earth and Planetary Science Letters* **395**, 254–266. https://doi.org/10.1016/j.epsl.2014.03.046.

Jeffery, A. J., Gertisser, R., Troll, V. R., Jolis, E. M., Dahren, B., Harris, C., Tindle, A. G., Preece, K., O'Driscoll, B., Humaida, H. et al. (2013). The pre-eruptive magma plumbing system of the 2007–2008 dome-forming eruption of Kelut volcano, East Java, Indonesia. *Mineralogie und Petrographie* **166**, 275–308.

Jolly, G., de la Cruz, S. (2015). Chapter 68 - Volcanic Crisis Management. In: Sigurdsson, H. (ed.) *The Encyclopedia of Volcanoes (Second Edition)*. Academic Press, pp. 1187–1202. https://doi.org/https://doi.org/10.1016/B978-0-12-385938-9.00068-7. ISBN 9780123859389.

Kadarsetia, E., Primulyana, S., Sitinjak, P. & Saing, U. B. (2006). Karakteristik kimiawi air danau kawah Gunung Api Kelud, Jawa Timur pasca letusan tahun 1990. *IJOG* **1**, 185–192.

Kahl, M., Chakraborty, S., Costa, F. & Pompilio, M. (2011). Dynamic plumbing system beneath volcanoes revealed by kinetic modeling, and the connection to monitoring data: an example from Mt. Etna. *Earth and Planetary Science Letters* **308**, 11–22.

Kahl, M., Chakraborty, S., Costa, F., Pompilio, M., Liuzzo, M. & Viccaro, M. (2013). Compositionally zoned crystals and real-time degassing data reveal changes in magma transfer dynamics during the 2006 summit eruptive episodes of Mt. Etna. *Bulletin volcanologique* **75**, 692.

Kilgour, G., Blundy, J., Cashman, K. & Mader, H. M. (2013). Small volume andesite magmas and melt–mush interactions at Ruapehu. *New Zealand: evidence from melt inclusions. Mineral Petrol* **166**, 371–392.

Kilgour, G. N., Saunders, K. E., Blundy, J. D., Cashman, K. V., Scott, B. J. & Miller, C. A. (2014). Timescales of magmatic processes at Ruapehu volcano from diffusion chronometry and their comparison to monitoring data. *Journal of Volcanological and Geothermal Research* **288**, 62–75.

Krimer, D. & Costa, F. (2017). Evaluation of the effects of 3D diffusion, crystal geometry, and initial conditions on retrieved time-scales from Fe–mg zoning in natural oriented orthopyroxene crystals. *Geochimica Cosmochimica Acta* **196**, 271–288.

Kristiansen, N. I., Prata, A. J., Stohl, A. & Carn, S. A. (2015). Stratospheric volcanic ash emissions from the 13 February 2014 Kelut eruption. *Geophysical Research Letter* **42**, 588–596.

Leake, B. E., Woolley, A. R., Arps, C. E., Birch, W. D., Gilbert, M. C., Grice, J. D., Hawthorne, F. C., Kato, A., Kisch, H. J., Krivovichev, V. G., Linthout, K., Laird, J., Maresch, W. V., Nickel, E. H., Rock, N. M., Schumacher, J. C., Smith, D. C., Stephenson, N. C. N., Ungaretti, L., Whittaker, E. J. W. & Guo, Y. (1997). Nomenclature of amphiboles report of the subcommittee on amphiboles of the international mineralogical association commission on new minerals and mineral names. *Can Mineral* **9**, 623–651.

Lesage, P. & Surono (1995). Seismic precursors of the February 10, 1990 eruption of Kelut volcano. *Clinical and Laboratory Standards Institute (Series)* **65**, 135–146.

Li, W., Costa, F. & Nagashima, K. (2021). Apatite crystals reveal melt volatile budgets and magma storage depths at Merapi volcano. *Journal of Petrology* **62**. https://doi.org/10.1093/petrology/egaa100.

Lloyd, A. S., Plank, T., Ruprecht, P., Hauri, E. H. & Rose, W. (2013). Volatile loss from melt inclusions in pyroclasts of differing sizes. *Contributions to Mineralogy and Petrology* **165**, 129–153. https://doi.org/10.1007/s00410-012-0800-2.

Lowenstern, J. B. (2001). Carbon dioxide in magmas and implications for hydrothermal systems. *Mineralium Deposita* **36**, 490–502. https://doi.org/10.1007/s001260100185.

Maeno, F., Nakada, S., Yoshimoto, M., Shimano, T., Hokanishi, N., Zaennudin, A. & Iguchi, M. (2019). A sequence of a plinian eruption preceded by dome destruction at Kelud volcano, Indonesia, on February 13, 2014, revealed from tephra fallout and pyroclastic density current deposits. *Journal of Volcanology and Geothermal Research* **382**, 24–41. https://doi.org/10.1016/j.jvolgeores.2017.03.002.

Mastin, L. G. & Witter, J. B. (2000). The hazards of eruptions through lakes and seawater. *Journal of Volcanological and Geothermal Research* **97**, 195–214. https://doi.org/10.1016/S0377-0273(99)00174-2.

Morgado, E., Morgan, D. J., Castruccio, A., Ebmeier, S. K., Parada, M. Á., Brahm, R., Harvey, J., Gutiérrez, F. & Walshaw, R. (2019a). Old magma and a new, intrusive trigger: using diffusion chronometry to understand the rapid-onset Calbuco eruption, April 2015 (Southern Chile). *Contributions to Mineralogy and Petrology* **174**, 1–11. https://doi.org/10.1007/s00410-019-1596-0.

Morgado, E., Morgan, D. J., Harvey, J., Parada, M. Á., Castruccio, A., Brahm, R., Gutiérrez, F., Georgiev, B. & Hammond, S. J. (2019b). Localised heating and intensive magmatic conditions prior to the 22–23 April 2015 Calbuco volcano eruption (southern Chile). *Bulletin of Volcanology* **81**. https://doi.org/10.1007/s00445-019-1280-2.

Müller, T., Dohmen, R., Becker, H. W., ter Heege, J. H. & Chakraborty, S. (2013). Fe-mg interdiffusion rates in clinopyroxene: experimental data and implications for Fe-mg exchange geothermometers. *Contributions to Mineralogy and Petrology* **166**, 1563–1576. https://doi.org/10.1007/s00410-013-0941-y.

Murphy, M. D., Sparks, R. S. J., Barclay, J., Carroll, M. R., Lejeune, A. M., Brewer, T. S., Macdonald, R., Black, S. & Young, S. (1998). The role of magma mixing in triggering the current eruption at the Soufrière Hills volcano, Montserrat, West Indies. *Geophysical Research Letter* **25**, 3433–3436.

Myers, M. L., Geist, D. J., Rowe, M. C., Harpp, K. S., Wallace, P. J. & Dufek, J. (2014). Replenishment of volatile-rich mafic magma into a degassed chamber drives mixing and eruption of Tungurahua volcano. *Bulletin of Volcanology* **76**, 1–17. https://doi.org/10.1007/s00445-014-0872-0.

Nakada, S., Bacon, C. R. & Gartner, A. E. (1994). Origin of Phenocrysts and compositional diversity in pre-Mazama Rhyodacite lavas, crater Lake. *Journal of Petrology* **35**, 127–162. https://doi.org/10.1093/petrology/35.1.127.

Nakamichi, H., Iguchi, M., Triastuty, H., Hendrasto, M. & Mulyana, I. (2019). Differences of precursory seismic energy release for the 2007 effusive dome-forming and 2014 Plinian eruptions at Kelud volcano, Indonesia. *Journal of Volcanology and Geothermal Research* **382**, 68–80. https://doi.org/10.1016/j.jvolgeores.2017.08.004.

Namur, O., Montalbano, S., Bolle, O. & Auwera, V. (2020). Petrology of the April 2015 eruption of Calbuco Volcano, Southern Chile. *Journal of Petrology* **61**, egaa084.

Neave, D. A. & Putirka, K. D. (2017). A new clinopyroxene-liquid barometer, and implications for magma storage pressures under Icelandic rift zones. *American Mineralogist* **102**, 777–794. https://doi.org/10.2138/am-2017-5968.

Norrish, K. & Hutton, J. T. (1969). An accurate X-ray spectrographic method for the analysis of a wide range of geological samples. *Geochimica Cosmochimica Acta* **33**, 431–453.

O'Neill, H. S. C. & Pownceby, M. I. (1993). Thermodynamic data from redox reactions at high temperatures. I. an experimental and theoretical assessment of the electrochemical method using stabilized zirconia electrolytes, with revised values for the Fe-"FeO", co-CoO, Ni-NiO and cu-Cu2O oxygen buffer. *Contributions to Mineralogy and Petrology* **114**, 296–314. https://doi.org/10.1007/BF01046533.

Pallister, J. S., Schneider, D. J., Griswold, J. P., Keeler, R. H., Burton, W. C., Noyles, C., Newhall, C. G. & Ratdomopurbo, A. (2013). Merapi 2010 eruption-chronology and extrusion rates monitored with satellite radar and used in eruption forecasting. *Journal of Volcanological and Geothermal Research* **261**, 144–152. https://doi.org/10.1016/j.jvolgeores.2012.07.012.

Pankhurst, M. J., Morgan, D. J., Thordarson, T. & Loughlin, S. C. (2018). Magmatic crystal records in time, space, and process, causatively linked with volcanic unrest. *Earth and Planetary Science Letters* **493**, 231–241. https://doi.org/10.1016/j.epsl.2018.04.025.

Pardini, F., Burton, M., Arzilli, F., La Spina, G. & Polacci, M. (2018). SO2 emissions, plume heights and magmatic processes inferred from satellite data: the 2015 Calbuco eruptions. *Journal of Volcanological and Geothermal Research* **361**, 12–24. https://doi.org/10.1016/j.jvolgeores.2018.08.001.

Pardyanto (1990). *Laporan Letusan Kelut 10 Februari 1990*. Indonesia: Direktorat Vulkanologi Pemerintah.

Passarelli, L. & Brodsky, E. E. (2012). The correlation between run-up and repose times of volcanic eruptions. *Geophysical Journal International* **188**, 1025–1045. https://doi.org/10.1111/j.1365-246X.2011.05298.x.

Patanè, D., De Gori, P., Chiarabba, C. & Bonaccorso, A. (2003). Magma ascent and the pressurization of Mount Etna's volcanic system. *Science* **299**(5615), 2061–2063. https://doi.org/10.1126/science.1080653.

Petrelli, M., El Omari, K., Spina, L., Le Guer, Y., La Spina, G. & Perugini, D. (2018). Timescales of water accumulation in magmas and implications for short warning times of explosive eruptions. *Nature communications* **9**, 1–14. https://doi.org/10.1038/s41467-018-02987-6.

Plail, M., Edmonds, M., Woods, A. W., Barclay, J., Humphreys, M. C. S., Herd, R. A. & Christopher, T. (2018). Mafic enclaves record syn-eruptive basalt intrusion and mixing. *Earth and Planetary Science Letters* **484**, 30–40. https://doi.org/10.1016/j.epsl.2017.11.033.

Putirka, K. (2016). Amphibole thermometers and barometers for igneous systems and some implications for eruption mechanisms of felsic magmas at arc volcanoes. *American Mineralogist* **101**, 841–858.

Putirka, K. D. (2008). Thermometers and barometers for volcanic systems. *Reviews in Mineralogy and Geochemistry* **69**, 61–120.

Rasmussen, D. J., Plank, T. A., Roman, D. C., Power, J. A., Bodnar, R. J. & Hauri, E. H. (2018). When does eruption run-up begin? Multidisciplinary insight from the 1999 eruption of Shishaldin volcano. *Earth and Planetary Science Letters* **486**, 1–14. https://doi.org/10.1016/j.epsl.2018.01.001.

Ratdomopurbo, A., Beauducel, F., Subandriyo, J., Nandaka, I. M. A., Newhall, C. G., Suharna, Sayudi, D. S., Suparwaka, H. & Sunarta (2013). Overview of the 2006 eruption of Mt. Merapi. *Journal of Volcanology and Geothermal Research* **261**, 87–97. https://doi.org/10.1016/j.jvolgeores.2013.03.019.

Ridolfi, F., Renzulli, A. (2012). Calcic amphiboles in calc-alkaline and alkaline magmas: Thermobarometric and chemometric empirical equations valid up to 1,130°C and 2.2 GPa. *Mineralogie und Petrographie* **163**, 877–895. https://doi.org/10.1007/s00410-011-0704-6

Ridolfi, F., Renzulli, A. & Puerini, M. (2010). Stability and chemical equilibrium of amphibole in calc-alkaline magmas: an overview, new thermobarometric formulations and application to subduction-related volcanoes. *Contributions to Mineralogy and Petrology* **160**, 45–66.

Samaniego, P., Le Pennec, J. L., Robin, C. & Hidalgo, S. (2011). Petrological analysis of the pre-eruptive magmatic process prior to the 2006 explosive eruptions at Tungurahua volcano (Ecuador). *Journal of Volcanological and Geothermal Research* **199**, 69–84. https://doi.org/10.1016/j.jvolgeores.2010.10.010.

Sauerzapf, U., Lattard, D., Burchard, M. & Engelmann, R. (2008). The titanomagnetite-ilmenite equilibrium: new experimental data and thermo-oxybarometric application to the crystallization of basic to intermediate rocks. *Journal of Petrology* **49**, 1161–1185. https://doi.org/10.1093/petrology/egn021.

Saunders, K., Blundy, J., Dohmen, R. & Cashman, K. (2012). Linking petrology and seismology at an active volcano. *Science* **336**(6084), 1023–1027.

Sharma, P. V. (1997). *Environmental and Engineering Geophysics*. Cambridge: Cambridge University Press, pp. 1–475. https://doi.org/10.1017/CBO9781139171168.002.

Sisson, T. W. & Bronto, S. (1998). Evidence for pressure-release melting beneath magmatic arcs from basalt at Galunggung, Indonesia. *Nature* **391**, 883–886. https://doi.org/10.1038/36087.

Sisson, T. W. & Grove, T. L. (1993). Experimental investigations of the role of H2O in calc-alkaline differentiation and subduction zone magmatism. *Contributions to Mineralogy and Petrology* **113**, 143–166. https://doi.org/10.1007/BF00283225.

Sjarifudin, M., Claproth, R. (1989). Prakiraan Tingkat Fraksinasi Magma Gunung Kelut Untuk Letusan yang akan Datan (1990?...). Indonesia: Direktorat Vulkanologi Pemerintah.

Smyth, H. R., Hamilton, P. J., Hall, R. & Kinny, P. D. (2007). The deep crust beneath island arcs: inherited zircons reveal a Gondwana continental fragment beneath East Java. *Earth and Planetary Science Letters* **258**, 269–282.

Spilliaert, N., Allard, P., Métrich, N. & Sobolev, A. V. (2006). Melt inclusion record of the conditions of ascent, degassing, and extrusion of volatile-rich alkali basalt during the powerful 2002 flank eruption of Mount Etna (Italy). *Journal of Geophysical Research: Solid Earth* **111**. https://doi.org/10.1029/2005JB003934.

Stock, M. J., Humphreys, M. C. S., Smith, V. C., Isaia, R. & Pyle, D. M. (2016). Late-stage volatile saturation as a potential trigger for explosive volcanic eruptions. *Nature Geoscience* **9**, 249–254.

Streck, M. J. (2008). Mineral textures and zoning as evidence for open system processes. *Reviews in Mineralogy and Geochemistry* **69**, 595–622. https://doi.org/10.2138/rmg.2008.69.15.

Sudradjat, A., Siswowidjoyo, S. (1993). Annual Report of the World Volcanic Eruptions in 1990. *Bulletin of Volcanology* **55**, 7–98. https://doi.org/10.1007/BF00301074.

Surono, J., Pallister, P., Boichu, J., Buongiorno, M., Budisantoso, M. F., Costa, A., Andreastuti, F., Prata F, S., Schneider, D., Clarisse, L., Humaida, H., Sumarti, S., Bignami, C., Griswold, J., Carn, S., Oppenheimer, C. & Lavigne, F. (2012). The 2010 explosive eruption of Java's Merapi volcano-a "100-year" event. *Journal of Volcanological and Geothermal Research* **241–242**, 121–135. https://doi.org/10.1016/j.jvolgeores.2012.06.018.

Thouret, J. -C., Abdurachman, K. E., Bourdier, J. -L. & Bronto, S. (1998). Origin, characteristics, and behaviour of lahars following the 1990 eruption of Kelud volcano, eastern Java (Indonesia). *Bulletin of Volcanology* **59**, 460–480.

Troll, V. R., Hilton, D. R., Jolis, E. M., Chadwick, J. P., Blythe, L. S., Deegan, F. M., Schwarzkopf, L. M. & Zimmer, M. (2012). Crustal CO_2 liberation during the 2006 eruption and earthquake events at Merapi volcano. *Geophysical Research Letter* **39**, 1–6. https://doi.org/10.1029/2012GL051307.

Vandemeulebrouck, J., Sabroux, J. -C., Halbwachs, M., Poussielgue, N., Grangeon, J., Tabbagh, J. et al. (2000). Hydroacoustic noise precursors of the 1990 eruption of Kelut volcano. *Clinical and Laboratory Standards Institute (Series)* **97**, 443–456.

Vernier, J. -P., Fairlie, T. D., Deshler, T., Natarajan, M., Knepp, T., Foster, K., Wienhold, F. G., Bedka, K. M., Thomason, L. & Trepte, C. (2016). In situ and space-based observations of the Kelud volcanic plume: the persistence of ash in the lower stratosphere. *J Geophys Res Atmos* **121**.

Wallace, P. J. (2005). Volatiles in subduction zone magmas: concentrations and fluxes based on melt inclusion and volcanic gas data. *Journal of Volcanological and Geothermal Research* **140**, 217–240. https://doi.org/10.1016/j.jvolgeores.2004.07.023.

Whelley, P. L., Newhall, C. G. & Bradley, K. E. (2015). The frequency of explosive volcanic eruptions in Southeast Asia. *Bulletin of Volcanology* **77**. https://doi.org/10.1007/s00445-014-0893-8.

Widiyantoro, S., Ramdhan, M., Métaxian, J. P., Cummins, P. R., Martel, C., Erdmann, S., Nugraha, A. D., Budi-Santoso, A., Laurin, A. & Fahmi, A. A. (2018). Seismic imaging and petrology explain highly explosive eruptions of Merapi volcano. *Scientific Reports* **8**, 1–7. https://doi.org/10.1038/s41598-018-31293-w.

Williams, G. T., Jenkins, S. F., Biass, S., Wibowo, H. E. & Harijoko, A. (2020). Remotely assessing tephra fall building damage and vulnerability: Kelud volcano. *Journal of Applied Volcanology* **9**, 1–18. https://doi.org/10.1186/s13617-020-00100-5.

Wirakusumah, A. D. (1991). Some studies of volcanology, petrology and structure of Mt. Kelut, East Java, Indonesia. Ph.D. Thesis in Research School of Earth Sciences, Victoria University of Wellington, New Zealand (Unpublished).